CHAPTER 5 DISTRIBUTION OF SEDIMENT IN UNDERFILLED BASINS

In the simplest of classifications, sedimentary basins consist of only two types, those filled predominately with sediment and those filled with water and sediment. In the first type, sediment delivered to the basin often is distributed by the same fluvial systems that carry it from the source. Only part of the sediment delivered from the source is trapped in the basin, the remainder being carried out by the drainage system which collects water and sediment from tributaries draining the basin's shoulders. Sedimentary sequences in these filled basins consist predominately of fluvial deposits with minor eolian and lacustrine contributions. The modern Andean foreland basin of Brazil is a good example. Deposition in these filled basins can be simulated with the models in the previous chapter and it is not necessary to discuss them further here.

Basins that are partly filled by lakes or epeiric seas usually trap most of the sediment delivered to them, and for this reason are here called "underfilled." Within them sediment is redistributed by various gravity-, wind-, and density-driven processes. Water flows of rivers entering a basin give way to density-driven flows of delta plumes, which in turn become dominated by wind-driven circulation and water surface waves. In deep waters, slides, slumps, and sediment gravity flows are important. The Arafura Sea between northern Australia and New Guinea is a modern example. Simulating underfilled basins requires a depositional model for each of these processes.

Here we present numerical models for these major processes that distribute sediment in underfilled basins. While the models all are simplified and two-dimensional, they nevertheless attempt to incorporate the physics of each process through the conservation laws. Deltas are treated first because they are located where the river load first leaves a confined channel. Depositional patterns in deltas depend on (1) water and sediment discharge, (2) wind-driven currents and waves, (3) tidal regime, and (4) a basin's geometrical form and bathymetry. Deltas

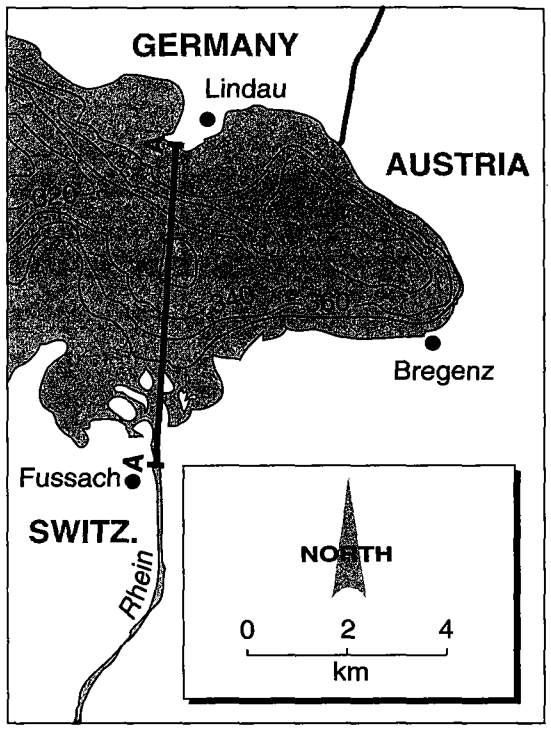

Figure 5-1
Eastern part of Lake Constance, Austria, showing delta formed where Rhine (Rhein) flows into Fussach Bay. Contours show elevation of bottom of lake in meters above sea level. Note trace of section of Figure 5-2 (after Muller, 1966).

dominated by the first three factors are called river-, wave-, and tide-dominated, respectively. A model for a river-dominated delta that incorporates a turbulent jet and sediment gravity flows is presented below.

Later, tides in channels and linear bays are treated using a form of St. Venant's equation which describes unsteady, nonuniform coastal channel flows in two dimensions. Then, tides and wind-driven currents of open seas are treated using a two-dimensional, vertically integrated model. Finally, wind-generated water surface waves are modeled using Airy wave theory.

DELTAS AND DELTA PROCESSES

The Rhine River, one of Central Europe's largest, originates in the Swiss Alps and flows northwestward into the North Sea. About 100 km from its source, it encounters a natural settling basin, Lake Constance, where more than 90 percent of the Rhine's sediment load at that point is deposited in a lacustrine delta. In 1900 the position of the mouth of the Rhine was artificially moved to Fussach Bay, in the eastern part of Lake Constance (Figure 5-1). This engineering feat inadvertently provided a natural laboratory for studying the growth of a new lacustrine delta. As of 1961, extension of the new Rhine delta had decreased the surface area of Lake Constance by about 1.2 km^2 (Figure 5-2). Approximately 26 million cubic meters of sediment were deposited between 1951 and 1961 alone (Figure 5-3). The growth has not been uniform in time however, because only modest growth occurred between 1941 and 1951 because of drought-induced low discharges of the Rhine. Note, too, that the delta is asymmetrical due to an artificial levee constructed on the east side of the river mouth that shunts distributaries to the west.

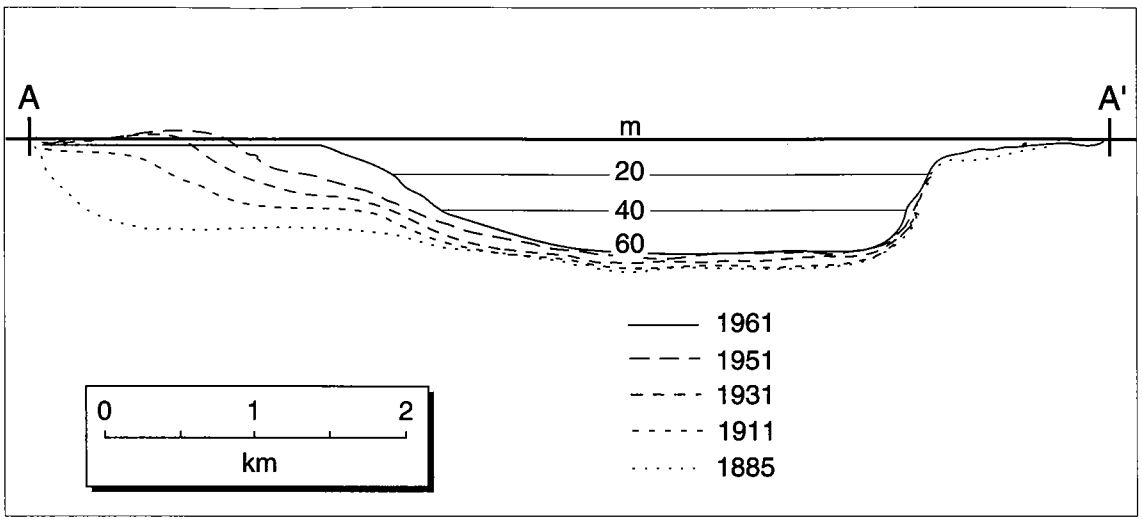

Figure 5-2 Profile showing growth of Rhine delta in Lake Constance (after Muller, 1966). See Figure 5-1 for trace of section.

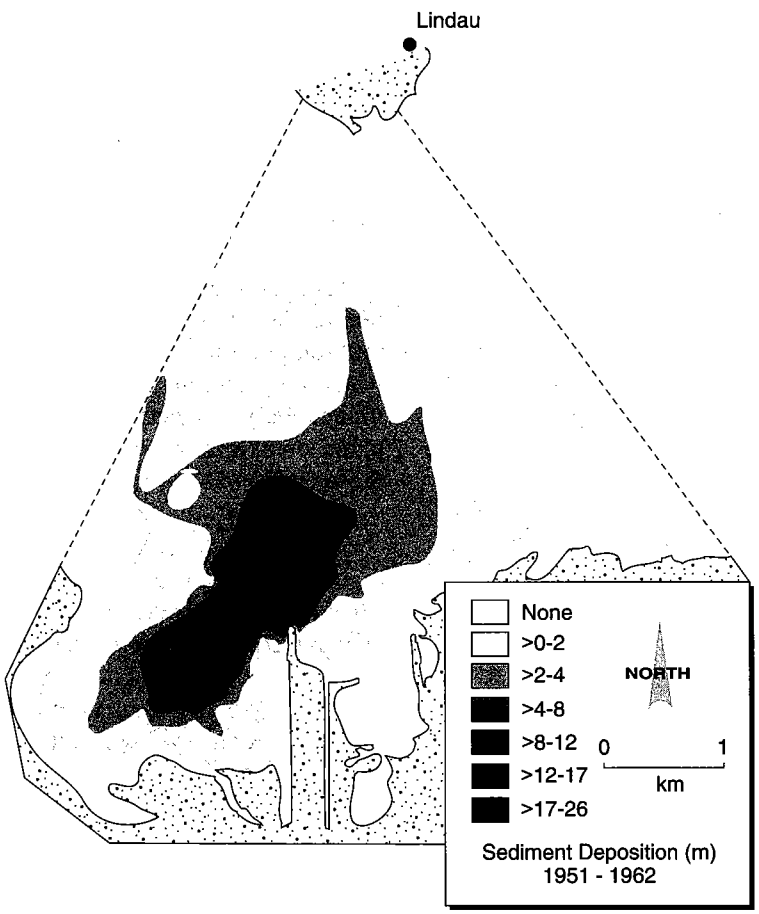

Figure 5-3
Thickness of deltaic sediments deposited between spring of 1951 and spring of 1961, Fussach Bay, Lake Constance, Austria (after Muller, 1966).

The morphology of the delta poses many questions. For example, what sedimentary processes and magnitudes have determined the concave-upwards shape of the delta front in Figure 5-2 and the planform of deposits shown in Figure 5-3? What are the expected sedimentary textures in the deposits? Answers to these questions can be obtained from a combination of field studies and numerical modeling.

First, field studies show that sedimentary patterns of river-dominated deltas arise from three distinct processes: sedimentation under an expanding turbulent jet; bedload dumping at the river mouth; and downslope gravity transport due to slumps, slides, and turbidity currents. The first two processes arise as flow expansion and entrainment of ambient fluid slows the river water, thereby reducing both its competency and capacity to carry sediment. Slumps, slides, and turbidity currents arise because of oversteepened slopes. To understand the mechanics of delta sedimentation requires quantifying each process. Although there are more sophisticated treatments, we follow the lead of James P. M. Syvitski and colleagues (1988) at Bedford Institute of Oceanography, Nova Scotia, and sacrifice detail for completeness. First, we provide a general model of flow in a turbulent jet and resulting bedload and hemipelagic sedimentation. Next, we model downslope gravity movements as a diffusion process. Finally, we combine the flow and sedimentation models in a conservation equation to predict the temporal evolution of the bed.

Deltas as Turbulent Jets

Turbulent jets are a special form of free turbulent shear flows in which turbulence is created by a flow shearing past relatively stagnant fluid, in contrast to flow past a fixed boundary. Typically, the mean flow velocity transverse to the main flow is very small compared with the main flow velocity. Also, changes of velocity and momentum in the direction of the main flow are slow with respect to those in the transverse direction.

The dominant driving force of turbulent delta jets may be either the momentum of the stream water or the water's buoyancy. The former is called a momentum jet, and the latter a plume. The buoyancy is created by less dense or warmer water flowing into more saline or colder water. Depending upon water depths immediately seaward of the stream mouth, the geometry of the jet will be either plane or axisymmetrical. Of course, actual delta distributaries are mixtures of these end members. Here we consider only a plane momentum jet (Figure 5-4).

The internal structure of a plane momentum jet consists of a development region with a seaward-tapering zone of flow in which velocity is constant that is surrounded by another region in which velocities decline laterally. Seaward is a fully developed region where radial profiles of axial velocity are similar from profile to profile. Both regions expand laterally at a linear rate with distance offshore due to turbulent entrainment of ambient fluid. Concurrently the maximum axial velocity decreases downstream due to loss of momentum and increasing cross-sectional area.

The fact that the velocity profile remains similar to itself along the various cross sections of the jet provides a useful simplification. Numerous laboratory studies have shown that the x-directed, transverse velocity profile is well approximated by a Gaussian, or normal distribution, function. Thus, in the zone of flow establishment the longitudinal velocity varies transversely as:

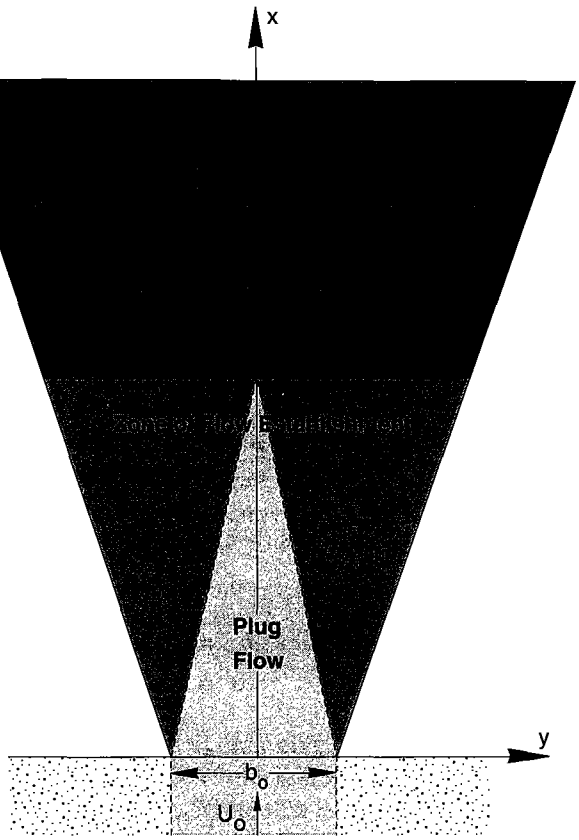

Figure 5-4 Schematic plan view of a plane turbulent jet. Zone of plug flow with constant velocity passes seaward into zone of established flow. U_o = flow velocity, b_o = stream width.

$$u_{x,y} = u_o \exp\left[-\frac{(y + ax - 0.5b_o)^2}{2\sigma^2}\right] \quad \textbf{(5-1)}$$

in the region

$$x \le \alpha^2 b_o \qquad \text{and} \qquad y > 0.5\,(b_o - \frac{x}{\alpha^2})$$

and

$$u_{x,y} = u_o \quad \textbf{(5-2)}$$

in the region

$$x \le \alpha^2 b_o \quad \text{and} \quad (-0.5\,(b_o - \frac{x}{\alpha^2}) < y < 0.5\,(b_o - \frac{x}{\alpha^2}))$$

In the zone of established flow the longitudinal velocity is given by:

$$u_{x,y} = u_o \alpha \left(\frac{b_o}{x}\right)^{\frac{1}{2}} exp\left[-\frac{y^2}{2\sigma^2}\right] \quad \textbf{(5-3)}$$

in the region

$$\alpha^2 b_o < x$$

where: $u_{x,y}$ = longitudinal velocity,

u_o = jet velocity leaving river mouth,

$a = \dfrac{\sqrt{\pi} C_1}{2}$,

b_o = channel width at river mouth,

σ = standard deviation of Gaussian velocity distribution,

$\alpha = \sqrt{\dfrac{1}{C_1 \sqrt{\pi}}}$,

C_1 = 0.109,

and x and y are as defined in Figure 5-4. Laboratory experimental data suggest that the rate of spreading is such that $\sigma = C_1 x$.

The y-directed velocities are obtained from the continuity equation for fluid within the jet. The continuity or conservation of mass equation for an incompressible fluid in the 2-D coordinate system of Figure 5-4 is obtained as follows. Consider a cell of water of thickness T, width dx, and length dy. Conservation of mass for this cell may be written as:

Time rate of change of mass in cell = mass rate in − mass rate out **(5-4)**

The left side of (5-4) may be written:

$$\frac{\partial \rho}{\partial t} T dx dy \quad \textbf{(5-5)}$$

where: ρ = fluid density.

The right side is obtained as follows. Mass may enter the cell along both the x and y directions. Considering the x direction first, mass enters the cell through the up-flow face at a rate given by $u\rho T dy$, where u is x-directed velocity. It exits the cell through the down-flow face at location $x+dx$, at a rate given by Taylor's theorem:

$$\text{mass rate out} = u\rho T dy + \frac{\partial}{\partial x}(u\rho T dy) dx \quad \textbf{(5-6)}$$

The y direction is treated similarly, and thus the net rate of mass addition (mass rate in – mass rate out) is:

$$-\frac{\partial}{\partial x}u\rho T dy dx - \frac{\partial}{\partial y}v\rho T dx dy \tag{5-7}$$

where: v = y-directed velocity.

Combining (5-5) and (5-7) as in (5-4), assuming the fluid is incompressible such that its density does not vary with location or time, and canceling like terms, yields:

$$\frac{\partial u}{\partial x} + \frac{\partial v}{\partial y} = 0 \tag{5-8}$$

To obtain v we first rewrite (5-8) as:

$$\frac{\partial v}{\partial y} = -\frac{\partial u}{\partial x} \tag{5-9}$$

Here one might consider obtaining v by substituting (5-1) through (5-3) respectively, into the RHS of (5-9), taking their derivatives with respect to x and integrating with respect to y. While this is possible in theory, in practice it is difficult. An easier method is to solve (5-9) directly by the finite-difference method.

Consider a flow field discretized into a rectangular mesh with nodes Δx and Δy apart (Figure 5-5). The x-directed velocities are known for all nodes, and, for

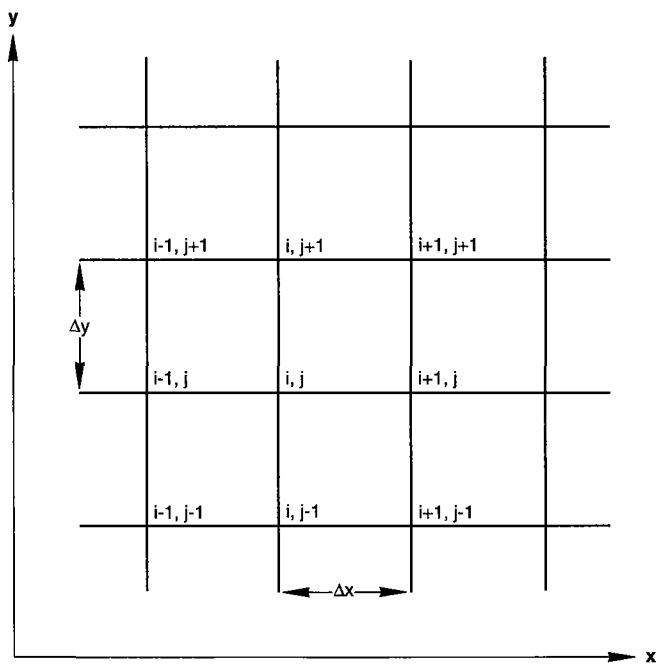

Figure 5-5 Example finite difference grid for obtaining y-directed velocities in 2-D turbulent plane jet.

argument's sake, assume that $v_{i,j}$, the y-directed velocity at i,j, also is known. The problem is to find $v_{i,\,j+1}$. The simplest finite difference approximation of the LHS of (5-9) is:

$$\frac{v_{i,j+1} - v_{i,j}}{\Delta y} \tag{5-10}$$

Now, Figure 5-5 shows that the gradient of u with respect to x that is mathematically and spatially equivalent to (5-10) should be at $j+1/2$, but u is not known there. The logical solution is to estimate u as an average of the u values at j and $j+1$, and then calculate the right-hand side of (5-9) as:

$$\frac{1}{2\Delta x}\left[\frac{[u_{i+1,j} + u_{i+1,j+1}]}{2} - \frac{[u_{i-1,j} + u_{i-1,j+1}]}{2}\right] \tag{5-11}$$

The two in the denominator arises because the x-directed velocities are chosen at $i+1$ and $i-1$, that is, at nodes $2\Delta x$ apart. Now, setting (5-10) equal to the negative of (5-11) as per (5-9), and solving for $v_{i,j+1}$, yields:

$$v_{i,j+1} = v_{i,j} + \frac{\Delta y}{4\Delta x}\left([u_{i+1,j} + u_{i+1,j+1}] - [u_{i-1,j} + u_{i-1,j+1}]\right) \tag{5-12}$$

Earlier, we assumed that $v_{i,j}$ was known. This will always be the case if the computation moves towards larger j values and if an initial value of v is provided. This initial value is easily specified because the symmetry of the plume requires that $v_{i,1}$, the y-directed velocity along the centerline, is always zero. Equations (5-1) through (5-3), and (5-12) provide the necessary equations for calculating the flow field of a 2-D, turbulent plane jet. They have been encoded in the FORTRAN subroutine of Program 15.

Having defined the flow field of a deltaic jet, we now can consider the sedimentation that occurs under it. This sedimentation consists of bedload dumping, emplacement by various gravity driven flows, and the settling of particles initially suspended within the river plume. These particles in the river plume consist of very fine sands, silts, and clays of terrigenous origin, as well as the remains of pelagic organisms, and hence are called hemipelagic sediments.

Hemipelagic Sedimentation Under the Jet

As the river jet decelerates and turbulence decays, particles begin to settle out. If the particles were all spheres of constant radius and known density, their settling velocities could be easily calculated using (4-53). But this is not the case. Particles also can fall as (1) sand and silt grains that are coated with clay particles, (2) clay clasts of silt size, (3) mineral-bearing fecal pellets of pelagic zooplankton with an average size of very fine sand, (4) silt-sized, inorganic floccules and colloidal floccules, and (5) biogenic tests. Collectively, these are called SPM, or suspended particulate matter.

The processes whereby SPM is formed and deposited are complex but work in fjords by Syvitski and colleagues (1988) has shown that the SPM deposition rate

can be predicted by a simple model that assumes particles are removed from the water column according to a first-order rate law. Consider a concentration C_o of SPM at a river mouth. The total inventory of SPM at the mouth, I_o, in kilograms per square meter, is C_o integrated over the channel depth H_o. Further assume that particles are removed from the water column at any point according to the first-order rate law:

$$\frac{dI}{dt} = -\lambda I \tag{5-13}$$

where: I = total mass of SPM in the water column per square meter,
λ = rate constant (t^{-1}).

Later, we will specify individual rate constants for each size, density, and shape of particle, but for now think of λ as an average rate constant for all SPM. Then the SPM remaining in the water column after time t, can be obtained by integrating (5-13) under the boundary condition $I = I_o$ at $t = 0$, thereby yielding:

$$I = I_o e^{-\lambda t} \tag{5-14}$$

If all of the material removed is deposited as sediment, then the sedimentation rate $Z(t)$ in kilograms per square meter per second is:

$$Z(t) = \frac{d}{dt}(I_o - I) = -\frac{dI}{dt} = \lambda I_o e^{-\lambda t} \tag{5-15}$$

It is sometimes preferable to define I_o in terms of the delivery rate of the suspended load to the river mouth:

$$I_o = H_o C_o = H_o \frac{Q_s}{Q_o} = \frac{Q_s}{u_o b_o} \tag{5-16}$$

where: Q_s = suspended load at river mouth (kg s^{-1}),
Q_o = river discharge at river mouth,
u_o = flow velocity at river mouth,
b_o = channel width at river mouth.

Substituting (5-16) into (5-15) yields:

$$Z(t) = \lambda \frac{Q_s}{u_o b_o} e^{-\lambda t} \tag{5-17}$$

Because the sedimentation rate of hemipelagic sediments in the plume is a function of time, we can predict the sedimentation rate at various points in front of the river mouth. This is accomplished by coupling the fluid velocity field of the

jet, derived in the previous section, with (5-17). If we assume that SPM travels at the same velocity as the fluid, then its location at time t is given by:

$$x = \int_0^t u dt \tag{5-18}$$

and

$$y = \int_0^t v dt \tag{5-19}$$

Thus, each point under the plume has a parcel of water above it that has taken a calculable amount of time t to reach the site. This time can be substituted into (5-17) to calculate the sedimentation rate there.

Earlier we noted that each particular size, density, and shape particle possesses a unique λ, because each has a specific settling velocity. Also, each is potentially affected by agglomeration, flocculation, and zooplankton pelletization, all of which may vary with time. We will assume that each size class has a specific, temporally invariant removal constant, λ_s. Thus, the total sedimentation rate at a site is the sum of the individual rates for each size class:

$$Z_T(t) = \sum \lambda_s \frac{Q_{s_s}}{u_o b_o} e^{-\lambda_s t} \tag{5-20}$$

Finally, the thickness of sediment deposited at a site after a time interval t equals:

$$D_s = \sum \frac{1}{\rho_{b_s}} \int_0^t Z_s dt \tag{5-21}$$

where: ρ_{b_s} = bulk density of s size fraction in kg m^{-3}.

These equations are incorporated in Program 16.

Bedload Dumping

Bedload dumping refers to the deposition of the fluvial bedload at the river mouth where flow expansion first reduces flow competency and capacity. The thickness of sediment deposited by this process per unit time and area is given by:

$$D_b = \alpha \frac{Q_b}{A \rho_b} \tag{5-22}$$

where: α = proportion of river bedload deposited beyond delta topset beds,
Q_b = bedload transport rate (kg s^{-1}),
A = area over which bedload is spread, here assumed to be given by width of river mouth times x_o(Figure 5-4),
ρ_b = bulk density of deposited bedload.

(5-22) is incorporated into a subroutine in the next section.

Downslope Diffusion

Processes such as slumping, which account for the bulk of sediment transported in many deltas, are difficult to define from first principles and so here are treated heuristically. We assume that the sediment transport rate S due to these processes is proportional to local bed slope:

$$S = -D \frac{\partial h}{\partial x} \tag{5-23}$$

where: D = transport coefficient (m^2 s^{-1}),
h = bed elevation,
x = distance.

From Chapter 4 the one-dimensional continuity equation for the bed is:

$$\frac{\partial h}{\partial t} = -\frac{\partial S}{\partial x} \tag{5-24}$$

which can be combined with (5-23) to yield:

$$\frac{\partial h}{\partial t} = D \frac{\partial^2 h}{\partial x^2} \tag{5-25}$$

This is the one-dimensional diffusion equation. Considering two dimensions and the addition of material at a rate R, from other processes such as bedload dumping yields:

$$\frac{\partial h}{\partial t} = D_x \frac{\partial^2 h}{\partial x^2} + D_y \frac{\partial^2 h}{\partial x^2} + R \tag{5-26}$$

Because (5-26) is used in a variety of disciplines, its solution has been well studied. An explicit finite-difference scheme is available for its solution but suffers from the drawback that the timestep must be less than some function of the space step to obtain a correct answer. It is better to proceed to the next level of complexity and consider an implicit finite-difference solution such as the Crank-Nicolson (CN) approximation.

Consider a grid of nodes where $x_i = i\Delta x$, and $y_j = j\Delta y$ and time is incremented as $t_k = k\Delta t$. Then the CN approximation to (5-26) is:

$$\left(\frac{h_{i,j}^{k+1} - h_{i,j}^{k}}{\Delta t} = \frac{D_x}{2(\Delta x)^2}\left[(h_{i+1,j}^{k+1} - 2h_{i,j}^{k+1} + h_{i-1,j}^{k+1}) + (h_{i+1,j}^{k} - 2h_{i,j}^{k} + h_{i-1,j}^{k})\right]\right)$$
$$+ \frac{D_y}{2(\Delta y)^2}\left[(h_{i,j+1}^{k+1} - 2h_{i,j}^{k+1} + h_{i,j-1}^{k+1}) + (h_{i,j+1}^{k} - 2h_{i,j}^{k} + h_{i,j-1}^{k})\right] \quad \textbf{(5-27)}$$
$$+ R_{i,j}^{k}$$

To calculate the updated value of the bed elevation at node i,j requires knowing the present bed elevations at the surrounding two nodes in the x and y directions *and the new bed elevations at those nodes.* The latter are not known yet, and therefore as things stand (5-27) is not solvable. But suppose that (5-27) is written for each node (i,j) at a given timestep over the ranges $i = 1, 2, \ldots m$, and $j = 1, 2, \ldots n$.This would yield m times n equations in m times n unknowns. The number of equations equals the number of unknowns, and the updated $h_{i,j}$ are theoretically calculatible. Of course the number of equations will easily reach the hundreds, and a computerized scheme for solving them is necessary.

Application of (5-27) is readily shown by example. Consider a three-by-three grid of nodes where elevations on the boundary nodes are known throughout time. Solution for the elevations at interior nodes proceeds by writing (5-27) for each node after separating all the unknown elevations—all the h^{k+1}—on the left side. The resulting set of equation in matrix notation is:

$$\begin{bmatrix}
1 & 0 & 0 & 0 & 0 & 0 & 0 & 0 & 0 \\
0 & 1 & 0 & 0 & 0 & 0 & 0 & 0 & 0 \\
0 & 0 & 1 & 0 & 0 & 0 & 0 & 0 & 0 \\
0 & 0 & 0 & 1 & 0 & 0 & 0 & 0 & 0 \\
0 & (-\theta_y) & 0 & (-\theta_x) & (1+2\theta_x+2\theta_y) & (-\theta_x) & 0 & (-\theta_y) & 0 \\
0 & 0 & 0 & 0 & 0 & 1 & 0 & 0 & 0 \\
0 & 0 & 0 & 0 & 0 & 0 & 1 & 0 & 0 \\
0 & 0 & 0 & 0 & 0 & 0 & 0 & 1 & 0 \\
0 & 0 & 0 & 0 & 0 & 0 & 0 & 0 & 1
\end{bmatrix}
\begin{bmatrix}
h^{k+1}{}_{1,1} \\ h^{k+1}{}_{2,1} \\ h^{k+1}{}_{3,1} \\ h^{k+1}{}_{1,2} \\ h^{k+1}{}_{2,2} \\ h^{k+1}{}_{3,2} \\ h^{k+1}{}_{1,3} \\ h^{k+1}{}_{2,3} \\ h^{k+1}{}_{3,3}
\end{bmatrix}
=
\begin{bmatrix}
H_{i,1} \\ H_{i,1} \\ H_{i,1} \\ H_{1,j} \\ F_{2,2}^{k} + \Delta t R_{2,2}^{k} \\ H_{3,j} \\ H_{i,3} \\ H_{i,3} \\ H_{i,3}
\end{bmatrix}
\quad \textbf{(5-28)}$$

where: $\theta_x = D_x\Delta t/(2(\Delta x)^2)$,

$\theta_y = D_y\Delta t/(2(\Delta y)^2)$,

H = known elevation,

$R_{i,j}^{k}$ = amount of increase in elevation over next timestep Δt due to other processes such as hemipelagic sedimentation,

$$F_{2,2}^{k} = \theta_x(h_{3,2}^{k} + h_{1,2}^{k}) + \theta_y(h_{2,3}^{k} + h_{2,1}^{k}) + (1 - 2\theta_x - 2\theta_y)h_{2,2}^{k}$$

With nine nodes there is only one interior node and it could be calculated explicitly. But with more interior nodes, the coefficient matrix of (5-28) will acquire five diagonal bands of nonzero terms. To solve for all the h values at the new timestep, an explicit calculation of $h_{i,j}^{k+1}$ is not possible. The equations must be solved simultaneously for the new bed elevations. (5-28) can be written in abbreviated matrix form as:

$$A \cdot h = b \qquad \textbf{(5-29)}$$

Here the dot denotes matrix multiplication, $\boldsymbol{A}$ is the coefficient matrix, $\boldsymbol{h}$ is the column vector of unknown elevations, and $\boldsymbol{b}$ is the column vector of known values from the right-hand side. To solve for $\boldsymbol{h}$, the coefficient matrix must be inverted and multiplied times the column matrix on the right side. While seemingly laborious, it requires only one-fourth the calculations of the explicit method and is numerically stable over all $\Delta t/\Delta x$ as well. Here we use a method of solution called LU decomposition as programmed in *Numerical Recipes* (Press, *et al*, 1986). Program 17 contains the FORTRAN code. Finally, all of the subroutines described above can be combined into a general model of delta sedimentation through the driver program listed in Program 18.

Experiment 5-1: Sedimentation in the Rhine Delta

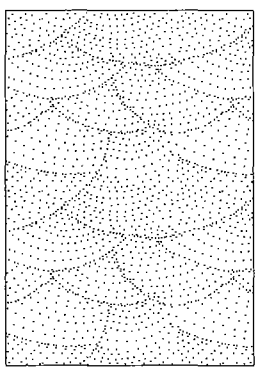

Earlier we posed two questions concerning the morphology of the Rhine Delta in Lake Constance. Now let us use the delta model to answer them. First, we need estimates of input parameters. Muller (1966) documented that the average water flow of the Rhine into Lake Constance from 1931 to 1960 was 224 m^3 per second, the average suspended load was 454 gm m^{-3}, and the average bedload was about 40,000 m^3 per year. The width of the channel was 200 m and the time-average depth about 4 m, giving an average flow velocity of 0.28 m per second. To account for the fact that roughly one-third of the sediment load exits through distributaries to the west and cannot be simulated by the model, we will reduce the suspended load by one-third. Values of the removal rate constant λ for the various size fractions in the hemipelagic model are obtained from the data of Syvitsky and others (1988). We also assume that the basin is deep enough so that the flow does not interact with the bed, and the basin waters are still except for circulation due to the jet. The flow field is discretized into a 20 by 22 square mesh, each cell 200 m on a side. The input file for the experiment is presented in Table 5-1 and results are shown in Figure 5-6.

Now we can answer the questions posed earlier. The flow expands in cross section as a linear function of distance into the basin, and decelerates as momen-

Table 5-1 Input data file for Experiment 5-1 involving turbulent plane jet of Rhine River as it enters Lake Constance.

```
im,jm,km: # nodes in x and y; # timesteps (I5) > 20<> 20<> 14<
Timestep in seconds (F10.3) >2.52288E08<
Spacestep in meters (F10.3) > 200.0 <
Flow velocity at river mouth (m/s) (F10.3) > 0.28 <
Width and depth of river mouth (m) (F10.3) > 200.0 < > 4.0 <
Diffusion constants in the x and y direction (F10.3) >0.00000001< > 0.00002 <
Elevation above datum (0.0) of sea level (m) (F10.3) > 60.0 <
Bedload dumping rate (m/s) (E10.3) > 6.0E-09 <
Concentration (gm/m**3) of coarse and med silt (F10.3)> 150.0 < > 50.0 <
Concentration (gm/m**3) of fine silt and clay (F10.3)> 50.0 < > 54.0 <
```

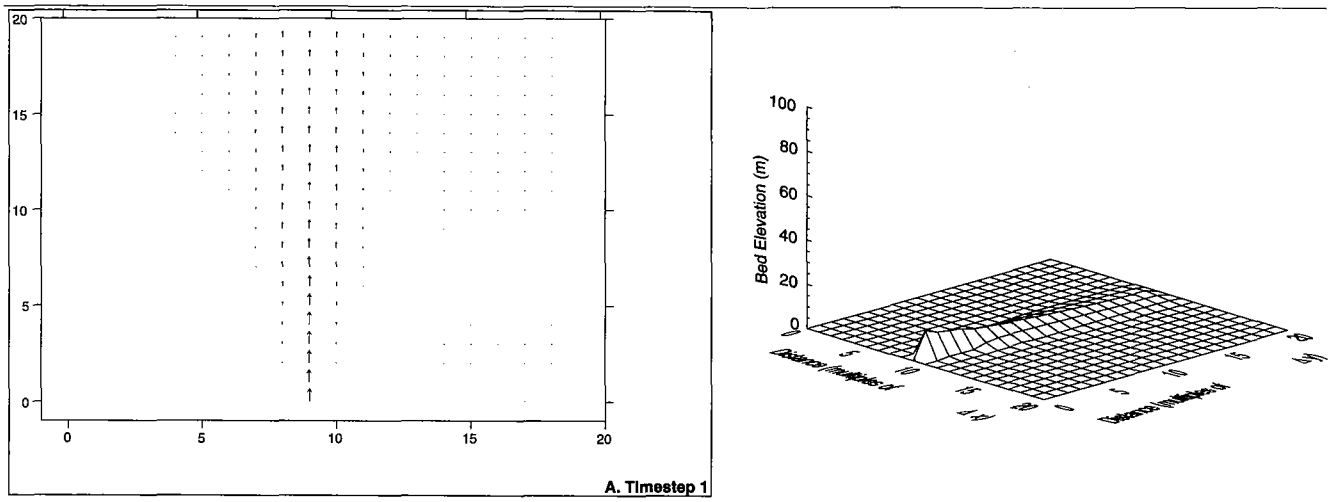

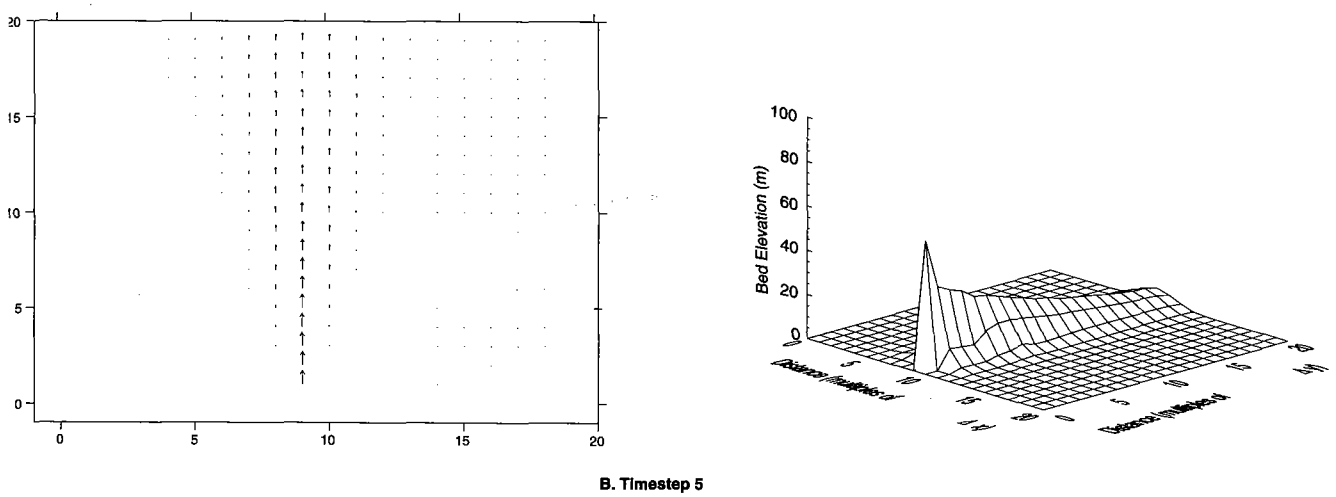

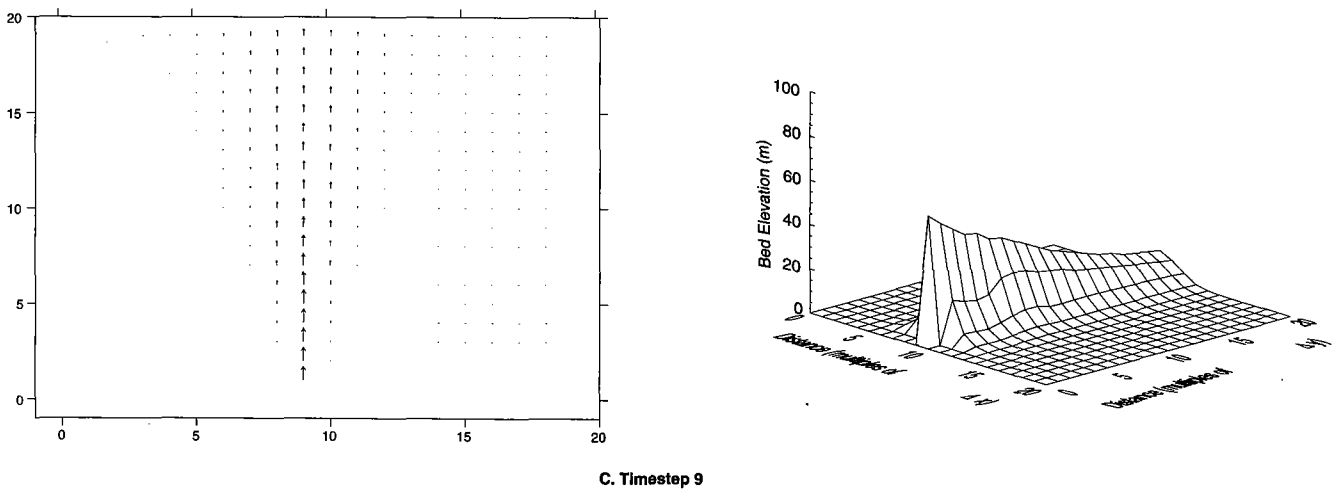

Figure 5-6 Maps of flow vectors and perspective diagrams of bed elevations (m above datum) computed from Experiment 5-1:Model of Rhine 2-D turbulent plane jet entering Lake Constance at 0.28 m s^{-1} at (A) timestep 1, (B) timestep 5, and (C) timestep 9.

tum of the jet is consumed in entraining and accelerating basin waters (Figure 5-6). The entrainment induces a symmetrical flow towards the jet, whose velocity far away from the jet is:

$$v_y = -0.155 \frac{v_o}{\sqrt{\frac{x}{b_o}}} \qquad \textbf{(5-30)}$$

As the delta progrades the flow field advances.

Sedimentation is most intense near the river mouth where the bedload is dumped and the rain of SPM is greatest. As the subaqueous portion of the delta grows upward to lake level, the river mouth advances and these sites of rapid deposition move lakeward. The shape of the subaqueous delta is a composite function of the path that fluid parcels take in the jet, the exponential decrease in SPM deposition with travel time, bedload dumping rate, and the x- and y-direction diffusion constants reflecting slumping and turbidity currents. The shape of the computed delta beds in Figure 5-6 would match those observed (Figure 5-2) only if the transverse diffusion constant is three orders of magnitude greater than the longitudinal diffusion constant. It is unlikely that slumping and turbidity currents preferentially travel transversely. More probably, wind-generated circulation in the basin spreads the plume. Because spreading is not treated explicitly in the model, it must be subsumed in the sediment-diffusion treatment.

UNSTEADY COASTAL CHANNEL FLOWS

Channelized flows in coastal environments include those in tidal channels that reverse with each tidal cycle, unidirectional flows of river distributaries, and combined flows in estuaries. These flows may be highly unsteady over periods ranging from minutes to days, with complex behavior that is counterintuitive. Flood waves may move down a distributary, or tidal waves move up an estuary. For these flows, the steady, gradually varied flow model in Chapter 4 is not adequate. Instead, a model employing St. Venant's equation describing long waves is required in addition to the continuity equation. A long wave, in this context, refers to long periods of oscillation, as found in tides, tsunamis, storm surges, seiches, surf beats, and flood waves. Below, we derive the St. Venant and continuity equations and apply them under the following assumptions:

- the channel is sufficiently straight and varies only gradually, such that a 1-D approximation is appropriate,
- flluid pressure is hydrostatic everywhere,
- the water surface slopes gently,
- fluid density does not vary,
- the resistance coefficient can be estimated by observations of uniform, steady flows,
- there are no lateral inflows along the channel, and
- the channel is narrow enough so that Coriolis accelerations may be ignored.

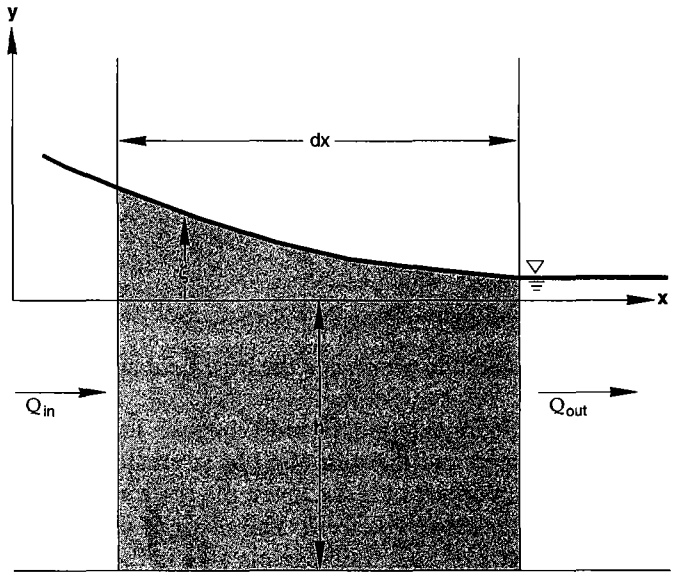

Figure 5-7 Longitudinal profile of stream occupying rectangular channel of width B, and cross-sectional area A. *X* axis is horizontal and in alongstream direction. Differential cell, stippled, has dimensions of B by h + ζ by dx, where h is still water depth and ζ is water surface elevation. Q is discharge.

Derivation of Model

Under these assumptions, the conservation of mass and momentum equations may be written using the notation of Figure 5-7. The conservation of mass or continuity equation states that the time rate of change of mass in a cell (stippled in Figure 5-7) equals mass flux in minus mass flux out, or:

$$\text{time rate of change of mass in cell} = \frac{\partial}{\partial t}[\rho\,(h+\varsigma)\,B]\,dx \qquad \textbf{(5-31)}$$

Mass flux in is ρQ, and mass flux out equals the mass flux in plus the amount by which that mass flux changes across the cell, or

$$\text{net flux} = \rho Q - \left[\rho Q + \frac{\partial}{\partial x}\rho Q dx\right] \qquad \textbf{(5-32)}$$

If we eliminate common terms, and assume that h (still water depth) does not vary with time, we obtain the conservation of mass equation:

$$\frac{\partial \varsigma}{\partial t} = -\frac{1}{B}\frac{\partial Q}{\partial x} \qquad \textbf{(5-33)}$$

The conservation of momentum equation, or general law of motion, states that the time rate of change of x-directed momentum in the cell equals the momentum flux into the cell minus momentum flux out, plus the sum of forces on the cell. The time rate of change of momentum of the cell fluid is the time rate of change of mass multiplied by velocity:

$$\frac{\partial}{\partial t}[\rho B\,(h+\varsigma)\,V]\,dx = \frac{\partial}{\partial t}\rho Q dx \qquad \textbf{(5-34)}$$

The momentum flux into the cell is the mass flux entering the cell multiplied by velocity. The momentum flux out equals momentum flux in, plus the amount by which that momentum flux changes across the cell, giving a net flux of:

$$[\rho B(h+\varsigma)V]V - \left[[\rho B(h+\varsigma)V]V + \frac{\partial}{\partial x}[\rho B(h+\varsigma)V]Vdx\right] = \frac{\partial}{\partial x}\rho QVdx \quad \textbf{(5-35)}$$

The forces acting on fluid in the cell are the net fluid pressure forces and the surface forces. The net pressure forces in the x direction arise because the hydrostatic pressure on one end of the cell will be different from that on the other end if the water surface tilts. The hydrostatic pressure p on the upstream side of the cell at any point in the vertical dimension, assuming uniform density, is:

$$p = p_a + \rho g(\varsigma - y) \quad \textbf{(5-36)}$$

On the downstream side of the cell, the pressure is that given by (5-36), plus the amount by which pressure has changed across the cell. The net pressure difference is:

$$-\rho g\frac{\partial \varsigma}{\partial x}dx \quad \textbf{(5-37)}$$

Here we assume that changes in atmospheric pressure p_a are negligible along the channel. Because the momentum equation is a force balance written in the x direction, the pressure terms must be multiplied by the area perpendicular to the x direction over which the pressure acts:

$$-\rho g(h+\varsigma)B\frac{\partial \varsigma}{\partial x}dx \quad \textbf{(5-38)}$$

The important surface force acting on the fluid in the cell is skin friction along the wetted perimeter, which may be represented by a shear stress τ_o multiplied by the area over which it acts Pdx, where P is the wetted perimeter. But from (4-20), τ_o equals ρgRS_f and because by definition PR equals A, the resistance term becomes:

$$-\tau_o Pdx = -\rho gRPS_f dx = -\rho gAS_f dx \quad \textbf{(5-39)}$$

which is negative, because it acts in the negative x direction. Assembling these terms yields:

$$\frac{\partial}{\partial t}\rho Qdx = -\frac{\partial}{\partial x}\rho QVdx - \rho g(h+\varsigma)B\frac{\partial \varsigma}{\partial x}dx - \rho gAS_f dx \quad \textbf{(5-40)}$$

If density does not vary in space or time, (5-40) may be divided through by ρ and dx. Writing V as $|V|$ to preserve the sign of the acceleration term, and writing $(h+\zeta)B$ as A, yields the final form of the momentum equation:

$$\frac{\partial Q}{\partial t} = -\frac{\partial}{\partial x}Q|V| - gA\frac{\partial \varsigma}{\partial x} - gAS_f \quad \textbf{(5-41)}$$

As developed in Chapter 4, S_f may be written in terms of V through the Chezy equation. Note also that the right-hand side of (5-41) is simply the gradually varied flow equation written in terms of discharge.

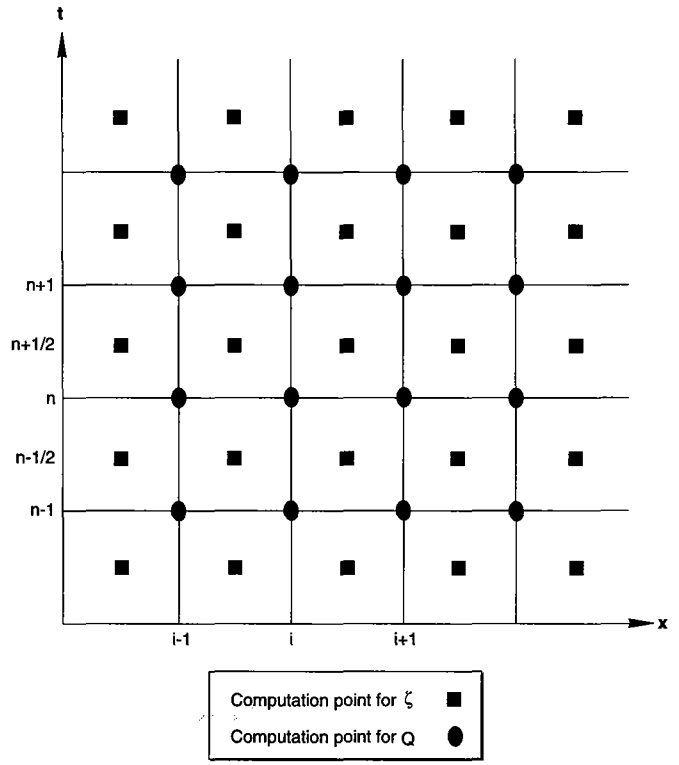

Figure 5-8 Computation points of finite-difference grid. Discharge Q, is computed at ith cross section and nth timestep, whereas water surface elevation ζ is computed at intermediate points in space and time.

An additional loss of momentum not yet accounted for occurs at abrupt channel enlargements as eddies are generated when boundary layers of the flow detach from the channel banks. We commonly assume that the head loss is proportional to change in velocity along stream through the channel enlargement:

$$\frac{\partial H}{\partial x} = \frac{\partial}{\partial x}\frac{V^2}{2g} \tag{5-42}$$

This head-loss term is a gradient or slope that may be included along with the friction slope in (5-41).

Equations (5-33) and (5-41) are two first-order, nonlinear, partial differential equations containing two dependent variables, Q and ζ, as functions of two independent variables, x and t. Like many formulas for natural flows, the set of equations cannot be solved analytically and numerical integration is required.

A numerical scheme, after Koutitas (1988), solves the finite-difference forms of (5-33) and (5-41) explicitly for ζ and Q at specific locations and times, or, as numerical analysts say, on a "staggered space-time grid" (Figure 5-8). The fact that values of dependent variables are known only at specific points in space and time is not as limiting as it may seem. Often we may know a channel's geometry only at a finite number of points and cannot specify continuous functions of B and

A for the equations anyway. The finite-difference forms of (5-33) and (5-41) are obtained by replacing the differentials with finite-difference quotients:

$$\frac{\varsigma_i^{n+\frac{1}{2}} - \varsigma_i^{n-\frac{1}{2}}}{\Delta t} = \frac{-2}{B_i + B_{i+1}} \left(\frac{Q_{i+1}^n - Q_i^n}{\Delta x} \right) \tag{5-43}$$

$$\frac{Q_i^{n+1} - Q_i^n}{\Delta t} = - \frac{\dfrac{(Q_{i+1}^n)^2}{A_{i+1}} - \dfrac{(Q_{i-1}^n)^2}{A_{i-1}}}{2\Delta x} - gA_i \frac{\varsigma_i^{n+\frac{1}{2}} - \varsigma_{i-1}^{n+\frac{1}{2}}}{\Delta x} - gA_i \left(\frac{(Q_i^n)^2}{\dfrac{A_i}{C^2 R_i}} + \frac{\left(\left| \dfrac{Q_{i+1}^n}{A_{i+1}} \right| - \left| \dfrac{Q_{i-1}^n}{A_{i-1}} \right| \right)^2}{4g\Delta x} \right) \tag{5-44}$$

where: n = current time step
i = current cross section or node number
Δx = finite space step
Δt = finite time step.

Notice in (5-43) that $\varsigma_i^{n+(1/2)}$ can be isolated on the left side, and in (5-44), Q_i^{n+1} can be likewise isolated. Thus values of the dependent variables at each new timestep may be obtained from their known values at the previous timestep. In other words, starting from some known initial conditions, the equations predict the future.

But it's not that simple. If you think of solving (5-33) and (5-41) as an exercise in the calculus, their integration yields two unknown functions, analogous to constants of integration for ordinary differential equations. Here, however, they are *functions* of integration because the equations are partial differential equations. We provide the information necessary to determine these functions as boundary conditions at the beginning and ending boundaries of the channel.

At the incident boundary, either the water surface elevation or discharge must be specified throughout the duration of the simulation. At the ending, or "terminating" boundary, we can allow the discharge to pass beyond the reach, or be zero. Thus the simplest set of boundary conditions is that ζ_1^t equals a known function and $Q_{i=\max}^t$ equals 0, where the superscript t indicates that this value holds over the whole time of the experiment. These boundary values provide the information that completely determines the result. If the known function is a tidal stage record and A, B, and C in (5-43) and (5-44) are appropriately chosen, then the equations coupled with the boundary conditions will simulate a tidal wave moving up an estuary as well as its reflection at the head of the estuary.

But another problem arises. Waves at the head of the channel will be reflected back along the channel to the incident boundary, where they must be allowed to pass out of the reach. If they do not, energy will accumulate unnaturally in the

reach, and the numerical solutions will become unstable. Thus, at the incident boundary, the water surface elevation ζ_1 must be the sum of an incident, known elevation of the water surface plus the elevation of the reflected wave. But how can we specify ζ_1 *a priori*? First, assume that we know the variation of the water's surface elevation imposed by incident waves traveling into the reach from a distance. For simplicity, suppose that the incident waves are sine waves of period T and amplitude ζ_o:

$$\varsigma_{in} = \varsigma_o \sin\left(\frac{2\pi n \Delta t}{T}\right) \tag{5-45}$$

where n is the counter for the time step. Then the elevation of the water surface at the boundary at the next time step, ζ_1^{n+1}, is:

$$\varsigma_1^{n+1} = \varsigma_o \sin 2\pi (n+1) \frac{\Delta t}{T} + \varsigma_{r_1}^{n+1} \tag{5-46}$$

where: $\varsigma_{r_1}^{n+1}$ = predicted water surface elevation of reflected waves at new timestep.

It is obtained by solving the wave equation:

$$\frac{\partial \varsigma}{\partial t} + C_o \frac{\partial \varsigma}{\partial x} = 0 \tag{5-47}$$

which, in finite-difference form is:

$$\varsigma_{r_1}^{n+1} = \varsigma_{r_1}^{n} + \frac{\Delta t}{\Delta x} C_o (\varsigma_{r_2}^{n} - \varsigma_{r_1}^{n}) \tag{5-48}$$

where: $\varsigma_{r_1}^{n}$ = water surface elevation due to reflected waves at node 1,

$\varsigma_{r_2}^{n}$ = water surface elevation due to reflected waves at node 2,

$C_o = \sqrt{g(h+\varsigma)}$.

Values for ζ_r are obtained in turn by assuming that they are the difference between the actual ζ computed at those nodes and the expected ζ from the incident waves:

$$\varsigma_{r_1}^{n} = \varsigma_1^{n} - \varsigma_{in_1}^{n} \tag{5-49}$$

$$\varsigma_{r_2}^{n} = \varsigma_2^{n} - \varsigma_{in_2}^{n} \tag{5-50}$$

Finally, expected ζ at those nodes is approximated from simple long-wave theory as:

$$\varsigma_{in_1}^{n} = \varsigma_o \sin\left(\frac{2\pi n \Delta t}{T}\right) \tag{5-51}$$

$$\varsigma_{in_2}^{n} = \varsigma_o \sin\left(\frac{2\pi n \Delta t}{T} - \frac{\Delta x}{L}\right) \tag{5-52}$$

where: $L = T\sqrt{g(h+\varsigma)}$.

Thus, the boundary condition at node 1, ζ_1, may be specified as a known sine function, while still allowing reflected waves to pass out through the incident boundary of the channel.

At the terminating boundary, the conditions are simpler. If it is a reflecting boundary, as at the head of an estuary, then $Q = 0$. If it is an open boundary, then the conservation principle for a moving surge applies:

$$V = \zeta\sqrt{\frac{g}{h}} \tag{5-53}$$

which may be used to calculate discharge at the last node using the finite difference form:

$$Q_{i_{\max}}^{n+1} = \zeta_{i_{\max}-1}^{n+\frac{1}{2}}\sqrt{gB_{i_{\max}}A_{i_{\max}}} \tag{5-54}$$

Equations (5-43) through (5-54) are encoded in Program 19 and applied to a channel of variable width and rectangular cross section where the slope of the water surface causes the flow, and where bed slope is unimportant. Input to the program consists of the number of cross sections, distance between each cross section Δx, number of timesteps, magnitude of each timestep Δt, Chezy friction factor C, period and amplitude of incident waves, whether the terminating boundary is reflecting or not, channel width B, and still-water depth h at each cross section. Except for Δx and Δt, we can choose any values of the above that do not violate the assumptions of the derivation. The space and time steps are constrained by a stability criterion called the Courant condition:

$$\frac{C_o\Delta t}{\sqrt{2\Delta x}} < 1 \tag{5-55}$$

where C_o has been defined above. The Courant condition decrees that the timestep must be less than the time needed for a perturbation to travel the distance between two nodes. Otherwise the solution becomes unstable, and ζ and Q become infinitely large or small.

Three Examples

We offer three examples of unsteady, gradually varied coastal flows, in order of increasing complexity, to stimulate appreciation of the rich behavior of these sedimentary processes.

Experiment 5-2: Influence of Chezy Friction Factor

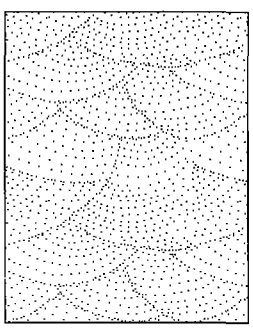

Consider a rectangular channel 2.5 km long and 30 m wide, with a still-water depth of 10 m everywhere. Simple water surface waves represented by a sine function enter at one end, with amplitudes of 1 m and period of 300 seconds, and exit the other end. To investigate the influence of bed friction on the waves, an experiment with an unusually low Chezy C of 5 $m^{1/2}/s$ is chosen, which compares with values of about 50 for various estuarine river mouths (Ippen, 1966). Table 5-2 constitutes the input file.

The output (Figure 5-9 and Color Plate 5-1) consists of surfaces, where one horizontal axis represents location along the channel x, and the other represents

Table 5-2 Input file for Experiment 5-3

```
25 1.0 100.0 5.0 300.0 1.0 1200 1 3 112 \IM,DT,DX,C,PR,ZO,NM,BK,MARK,NWRITE
30 30 30 30 30 30 30 30 30 30 30 30 30 30 30 30 30 30 30 30 30 30 30 30 30 \B(I)
10 10 10 10 10 10 10 10 10 10 10 10 10 10 10 10 10 10 10 10 10 10 10 10 10 \HO(I)
```

time t. The vertical axis represents water-surface elevation ζ. In Figure 5-9, each section whose trace is perpendicular to the distance axis represents a cross section of the channel, and each section perpendicular to the time axis represents a "time slice." As shown, waves enter the channel with an amplitude of 1 m, but they attenuate dramatically and deform into asymmetrical square waves as they propagate down the channel (diagonally in x-t space). Simplified analytical solutions of (5-33) and (5-41) (Ippen, 1966) demonstrate that frictional attenuation follows an exponential decay function. The deformation, seen at the end of the channel in Color Plate 5-1, arises because the wave crest travels faster than the trough. This is a consequence of the fact that shallow water waves, even in the absence of friction, travel with celerity or speed C_o, as defined above. In addition, the friction term in (5-41) is inversely proportional to water depth, so that crests encounter slightly less frictional resistance than troughs. The net result is deformation of the wave form.

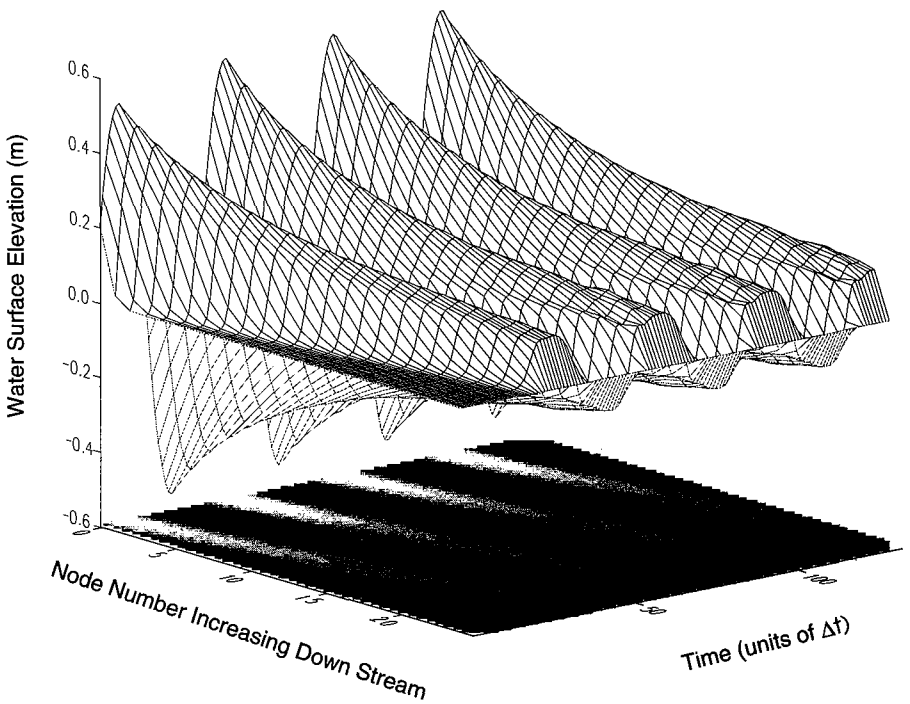

Figure 5-9 Computed water surface elevations for Experiment 5-3. Simple sinusoidal water wave is imposed at incident boundary of channel. Wave crest propagates downstream over time and passes diagonally across space-time plane, exiting at lower right edge of surface. Wave is dampened and distorted to form partially square wave as function of bed friction.

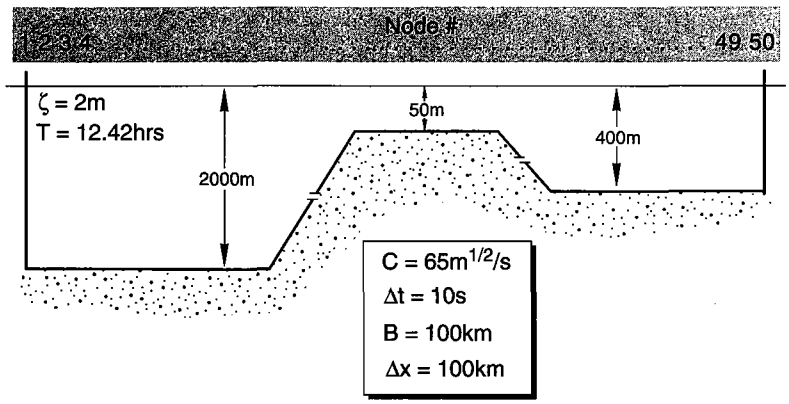

Figure 5-10 Schematic traverse used in Experiment 5-3. Numbers denote individual cross sections perpendicular to traverse. Tidal waves enter from open ocean on left and pass over sill, entering an epicontinental sea on right. ζ is incident tidal amplitude, T is tidal period, C is Chezy coefficient, Δt is timestep, B is cross-section width, and Δx is distance between cross sections.

Experiment 5-3: Influence of Submerged Shelves on Tidal Waves

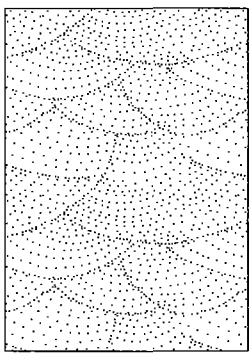

Ancient epicontinental seas often were separated from open oceans by shallow carbonate platforms or shelves, as for example, in the Albian (Cretaceous) interior seaway of western North America. Others were separated from the open ocean by tectonic sills. These barriers undoubtedly had strong effects on the propagation of tidal waves, and in turn on the sedimentary environments both within and along the margins of the sea. The wave model outlined above provides an opportunity to investigate this effect. Interestingly, the width of the shelf relative to the tidal wavelength, more than the water depth, determines the tidal energy that passes over the barrier into the epicontinental sea.

Consider an entrance to an epicontinental sea that is 100 km wide and with bathymetry depicted in Figure 5-10. Assume, also, that a simple, semidiurnal, lunar (M_2) tide (T = 12.42 hours, ζ_o= 2 m) propagates into the epicontinental sea from the open ocean. What changes in tidal range and velocities will the barrier induce? We can devise an experiment using the input file in Table 5-3.

The solutions for water surface elevation ζ are presented in Figure 5-11 and compared with those for an equivalent situation except that the water depth is

Table 5-3 Input file for Experiment 5-3

```
50 10.0 100000.0 65.0 44712.0 2.0 26828 1 3 112
100000. 100000. 100000. 100000. 100000. 100000. 100000. 100000. 100000. 100000.
100000. 100000. 100000. 100000. 100000. 100000. 100000. 100000. 100000. 100000.
100000. 100000. 100000. 100000. 100000. 100000. 100000. 100000. 100000. 100000.
100000. 100000. 100000. 100000. 100000. 100000. 100000. 100000. 100000. 100000.
100000. 100000. 100000. 100000. 100000. 100000. 100000. 100000. 100000. 100000.
2000. 2000. 2000. 2000. 2000. 2000. 2000. 2000. 2000. 2000. 2000. 2000. 2000.
2000. 2000. 2000. 2000. 2000. 2000. 2000. 2000. 2000. 2000. 2000. 2000. 2000.
2000. 2000. 2000. 2000. 2000. 2000. 2000. 2000. 1610. 1220. 830. 440. 50. 50.
50. 180. 400. 400. 400. 400. 400. 400. 400. 400.
```

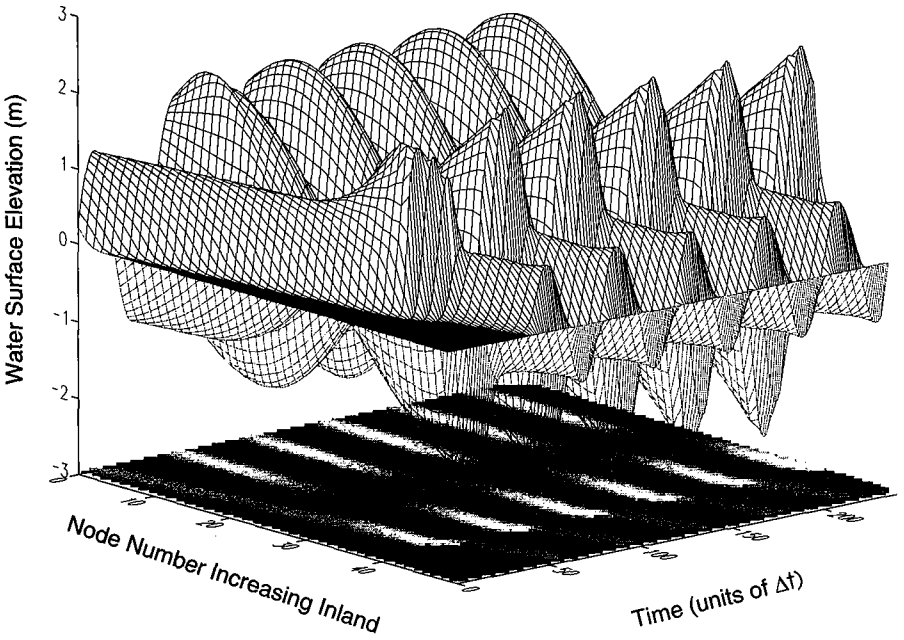

Figure 5-11 Computed water surface elevations for Experiment 5-3. Equilibrium tides show amplification over sill due to convergence and superposition of incident and reflected waves, and a dampened wave in epicontinental sea, due to loss of wave energy by reflection.

2000 m everywhere (Figure 5-12).The space-time diagram (Figure 5-11) shows that a tidal wave crest initially travels into the epicontinental sea, moving diagonally across the space-time surface, while maintaining uniform height and wave speed or celerity. Celerity is given by the slope of the propagation path on the space-time plane. Each time line represents 1120 seconds (18.67 minutes), and each space line is 100 km. The wave travels about ten "space lines" in six "time lines," or about 148 m/s. Given the range of error in our estimate based on Figure 5-11, this result is not much different from the speed of an ideal, frictionless shallow water wave as given by C_o (see definitions for (5-48)), which is about 140 m/s.

When the wave reaches the sill, its height increases and its celerity decreases (Figure 5-11). The increase in wave height is caused by convergence effects and by reflection of wave energy off the seaward face of the sill. Let us consider the convergence effects first. The total potential and kinetic energy per unit surface area of a long wave is:

$$E = \frac{\gamma a^2}{2} \tag{5-56}$$

where: γ = specific gravity of water

a = amplitude of wave.

Therefore the total energy of a wave is E times the crest length (call it l) and wavelength L, as defined for (5-52). Now consider a wave propagating into shallow water. If we assume, as a first approximation, that the total energy of the wave

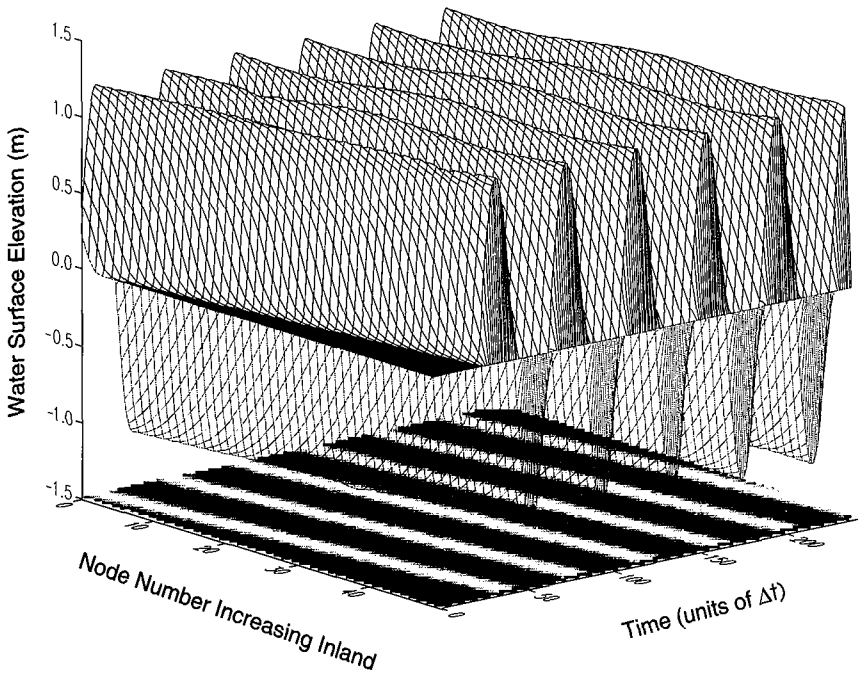

Figure 5-12 Computed water surface elevations for Experiment 5-3, with water 2000 m deep. In absence of sill, tidal waves propagate into seaway with little change in form.

remains unchanged as it travels, then its energy at any site in deeper water (call it site 1) will equal the energy at a site in shallower water (site 2), or:

$$\frac{\gamma a_1^2}{2} l_1 T \sqrt{g\,(h_1+\zeta_1)} = \frac{\gamma a_2^2}{2} l_2 T \sqrt{g\,(h_2+\zeta_2)} \tag{5-57}$$

or,

$$\frac{a_2}{a_1} = \left(\frac{l_1}{l_2}\right)^{\frac{1}{2}} \left(\frac{h_1+\zeta_1}{h_2+\zeta_2}\right)^{\frac{1}{4}} \tag{5-58}$$

This is Green's law, named after an obscure, self-taught miller's son, George Green, who derived it in 1837 (Lamb, 1945). In Experiment 5-3 above, site 1 would be in water 2000 m deep and site 2 in water 50 m deep, with l_1 equal to l_2. From (5-58), the tidal amplitude at site 2 should be about 2.5 times that at site 1, not because of friction and reflection of wave energy but simply due to convergence effects.

The reflected wave appears as a wave crest traveling back to sea at roughly the same velocity (angle in the space-time plane) as the incident wave. The reflected wave is superimposed on the next wave entering the epicontinental sea, producing a water-surface elevation at cross section 6 of about 2.2 m above mean water level

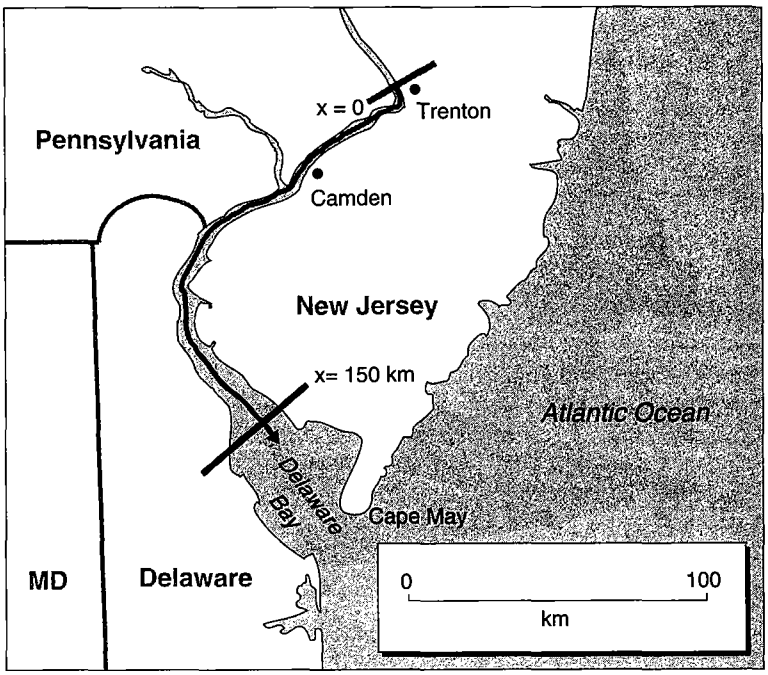

when the wave crests coincide. Figure 5-11 shows that superposition of the reflected and incident waves produces a complex tidal pattern in front of the sill, which may be thought of as a combination of progressive and standing waves.

Behind the sill, the tidal wave's amplitude is attenuated to about 0.9 m and is shifted in phase by about 1-1/4 hours (Figure 5-11), with celerity slowed to about 62 m/s, which is consistent with the shallower depths. The attenuation is caused by the wave reflection in front of the sill. Assuming for the moment that the tidal wave's loss of internal energy is small as it passes over the sill, then the law of conservation of energy decrees that the transmitted wave's energy must equal the incident wave's energy minus reflected energy. As presented above, the energy per unit surface area of a wave is proportional to the square of the amplitude. The amplitude of the transmitted wave a_t therefore is:

$$a_t = \sqrt{a_i^2 - a_r^2} \tag{5-59}$$

The attenuation is a function of the water depth in front of, over, and behind the barrier, as well as the barrier's width relative to wavelength L. As Koutitas (1988) points out, as the width of the barrier approaches L, the transmitted wave amplitude approaches zero. The sensitivity of wave amplitude to the barrier's width and depth can readily be explored by varying its bathymetry in the input file.

These results help us interpret sedimentation behind sills, banks, and bars. For example, Ericksen and Slingerland (1990) point out that tidal circulation probably was much less important than wind-driven circulation in the interior seaway of western North America during Albian time. Their simulations suggest that frictional dissipation and reflection due to the Texas carbonate bank at the seaway's southern entrance dampened Tethyian tides in the seaway.

Experiment 5-4: Behavior of Tides in Delaware Bay

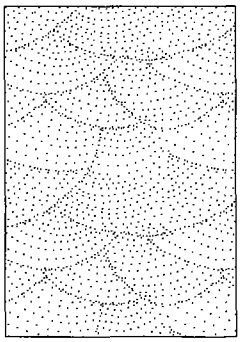

Figure 5-13
Map of Delaware Bay. Reach modeled in Experiment 5-4 extends about 150 km down estuary from Trenton.

Delaware Bay, on the Atlantic coast of the United States (Figure 5-13), is an estuary formed by post-glacial drowning of the Delaware River valley over the last 18,000 years. It extends about 215 km from its head at the fall line at Trenton, New Jersey, to its mouth at Cape May. Although predominately saline, it receives fresh water from the Delaware and Schuylkill rivers. It is also subject to tides of the Atlantic Ocean of predominantly M_2 type as defined in Experiment 5-3. Like many river mouths that are influenced by tides, its upper two-thirds is funnel shaped and is thus representative of ancient estuaries in which tidal waves of the open ocean induced complex tides within the estuaries. As in Experiment 5-3, tidal circulation in estuaries of this type is influenced by the lateral convergence of the tidal crest and by reflection from the estuary head and sides. A model of Delaware Bay provides further insight into complex circulations and provides a test of how well the model simulates reality. We will focus on the funnel-shaped upper two-thirds of the estuary, although in principle we could apply the model to the entire length of the estuary, beginning at its entrance to the Atlantic.

The hydraulic geometry of upper Delaware Bay (Ippen, 1966) is well represented by equations of the form:

$$B = 1000e^{\delta x} \text{ (ft)} \tag{5-60}$$

$$A = 21,000e^{\delta x} \text{ (ft}^2\text{)} \tag{5-61}$$

where: $\delta = 0.67 \times 10^{-5}$ ft^{-1}
$x = 0$ at Trenton.

The mean depth, $\bar{h}$, is A/B, or 21 ft (6.4 m). These equations generally apply moving down the estuary to where $x = 5 \times 10^5$ ft (Figure 5-13). The tidal amplitude a_x at any distance x relative to the amplitude a_o at $x = 0$ (Figure 5-14) decreases and then increases as the wave travels up the estuary, reaching a maximum at Trenton, where $a_o = 1$ m. High water at Trenton is 5.6 hours after high water at the entrance (Ippen, 1966).

In our simulations of upper Delaware Bay, it is convenient to define a curved traverse or line-of-section along its axis, and in turn subdivide it into 50 cross sec-

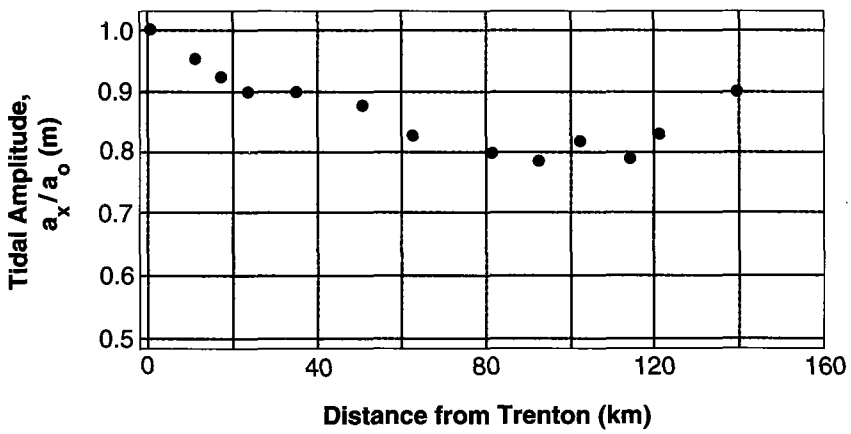

Figure 5-14 Observed tidal amplitude ratios versus distance from Trenton in Delaware Bay, where observed tidal amplitude, a_o, is 1 m.

Table 5-4 Input data file for Experiment 5-4

```
51 10.0 3048.0 38.0 44712.0 1.9 50000 0 3 112 \IM,DT,DX,C,PR,ZO,NM,BK,MARK,NWRITE
```

tions. The width and area of each cross-section are calculated from (5-60) and (5-61) and converted to meters. Mean depth is 6.4 m everywhere, and a timestep of 10 seconds is employed, as calculated from (5-55). The entrance tides to the reach are simulated by a sine function of period 12.42 hours (Harleman, 1966). The amplitude ζ_o of the entrance tides is difficult to specify at the beginning of the experiment, because we have chosen the boundary inside the estuary. The observed actual tidal amplitude at the boundary is 0.9 m (Figure 5-14), but this is the sum of an incident wave and a wave reflected off the estuary head. We could compute the incident amplitude by subtracting the reflected amplitude from the observed amplitude, but the amplitude of the reflected wave is not known and must be calculated by the model. There is an additional uncertainty, because we also do not know the Chezy C. The solution, however, is to conduct a number of experiments, varying ζ_o and C, until the computed amplitudes match the observed. This may seem to defeat the purpose of the modeling, but we do obtain additional information, including the shape of the tidal wave, its phase change as it progresses up the estuary, and most importantly, an explanation for the curious spatial variations in its amplitude.

We will also simulate the situation in the autumn months, when the discharge of fresh water is lowest and can be ignored in the model. Table 5-4 contains the input file for the specific experiment whose results best fit the observed amplitudes. Unlike the input files of previous experiments, the input file does not contain the widths and depths of the individual cross sections. These are calculated within a version of the program modified from Program 19.

From the results graphed in Figure 5-15 and Figure 5-16 we first note that the calculated tidal amplitude ratios closely match the observed. The incident amplitude and Chezy C that produce this close correspondence (Table 5-4) are reasonable, although the Chezy C is low compared with other estuaries. For example, River Hoogly in India has a Chezy C of 67 $m^{1/2}/s$. A low C value represents a high rate of energy loss due to friction, which arises because we have forced the friction term in (5-44) to account for energy losses from continuous reflection of wave energy off lateral boundaries, as well as dissipation by bed friction. Secondly, the phase changes match equally well. The predicted time of high tide at Trenton is slightly more than five hours after high tide at the entrance, comparing favorably with the observed lag of 5.6 hours (Ippen, 1966).,

How shall we explain this phase lag and variations in amplitude with distance up the estuary? The model helps answer this question by exploring the influence of wave reflection in the absence of crestal convergence, and vice versa. Figure 5-17 presents model results for a situation in which the estuary is of a uniform width equal to that of Delaware Bay's width at Trenton. The reflected wave now shows clearly. Frictional dissipation dampens both the incident and reflected waves, and when the two wave heights are summed, they yield an amplitude-ratio curve of the correct shape but whose magnitudes are too low.

Another experiment in which the funnel shape of Delaware Bay is included, but not wave reflection, shows that funneling causes a monotonic rise in tidal amplitude up the estuary. When the two effects are superimposed, a frictionally

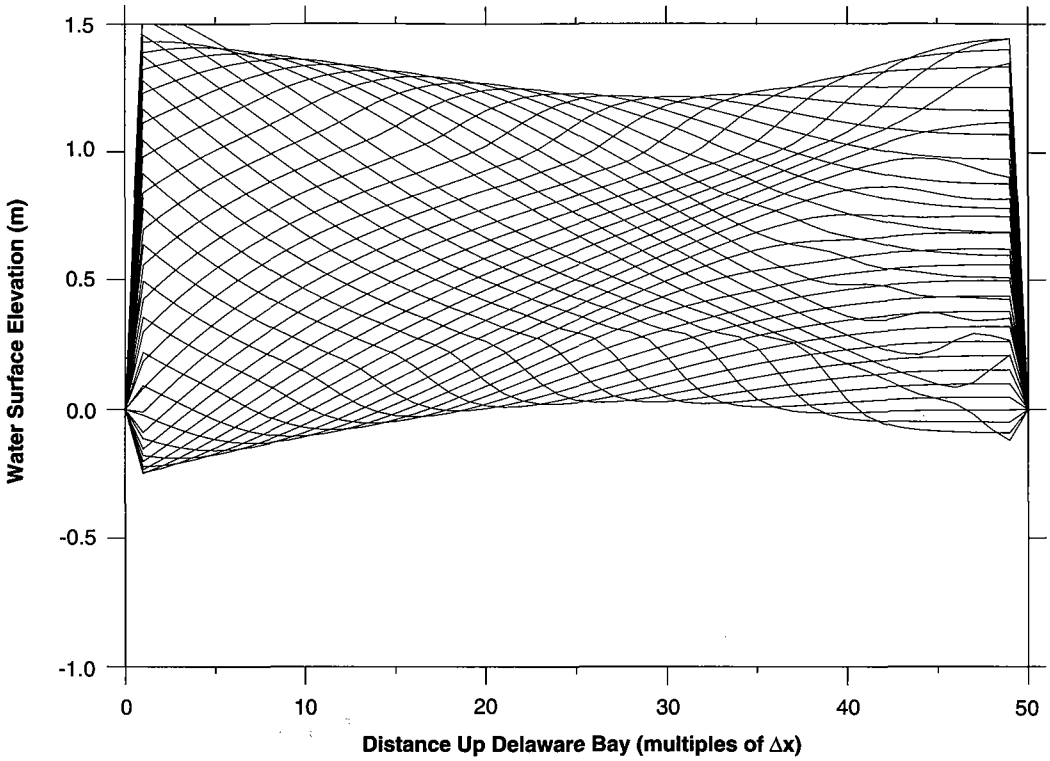

Figure 5-15 Computed water surface elevations over tidal cycle for Experiment 5-4. Each line represents water surface elevation at an instant. Difference between highest and lowest elevations at a point is tidal range. $\Delta x = 3.048$ km.

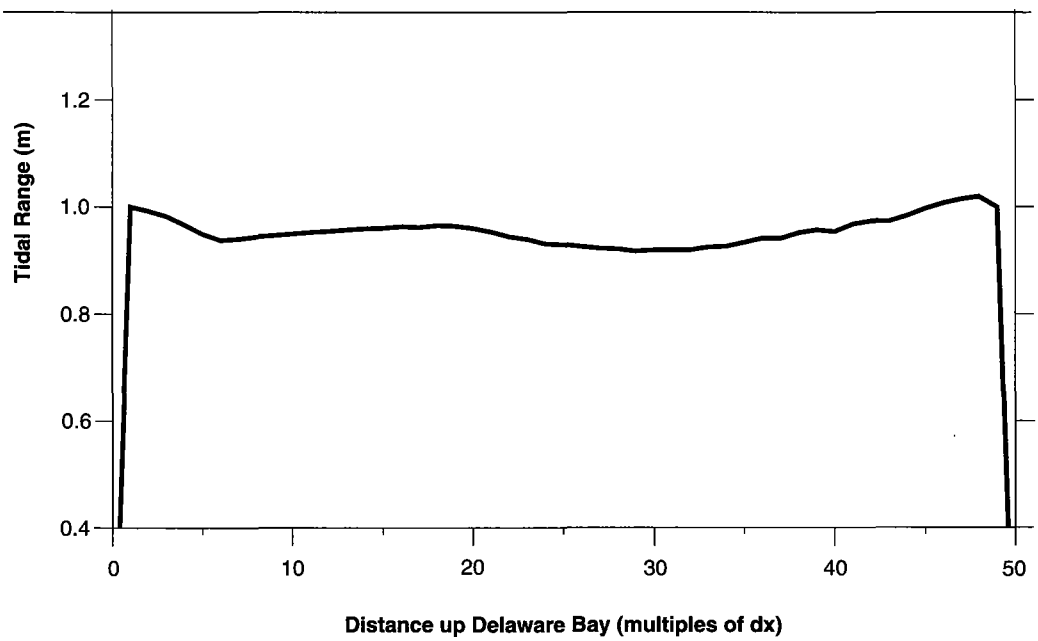

Figure 5-16 Computed tidal range (relative to the range at Trenton) versus distance along estuary. Values upon which plot is based compare favorably with observed values in Figure 5-14.

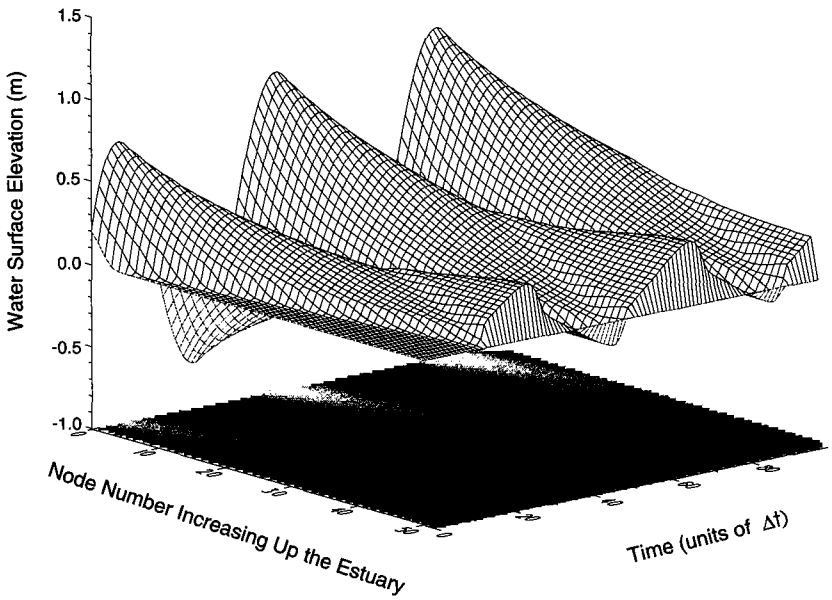

Figure 5-17 Computed water surface elevation for Experiment 5-4, with estuary of constant width. Waves travel up estuary (towards lower right) and are reflected off estuary head at Trenton (lower right edge of surface). Both incident and reflected waves are frictionally damped, and their superposition produces some of change of tidal amplitude with distance seen in Figure 5-15. Remainder is due to convergence.

damped, reflected wave develops that is augmented due to funneling. The resulting variations of amplitude with distance up the estuary (Figure 5-14) would be difficult to predict in the absence of modeling. The tides in many other estuaries behave similarly. It is not the funneling effect but the reflected wave that plays the major role in causing macrotides.

2-D, UNSTEADY, NONLINEAR TIDAL AND WIND-DRIVEN COASTAL CIRCULATION

Introduction

Many epicontinental sedimentary basins contained shallow seas at times in their history. To interpret deposits formed in these seas, we must "hindcast" their oceanography and focus on questions such as were there net sediment transport directions, were they tide- or wind-dominated, and were salinity gradients important. Numerical models help because they allow the geologist to conduct sensitivity experiments. The logic for their use is as follows: If the paleobathymetry and paleogeography of a basin can be specified, and if the incident tides from the open ocean can be specified, and if the sea was not stratified, then physical laws embodied in the geophysical flow equations demand that the circulation must have assumed the computed form. Such a hindcast can then be tested against field data. If the match is poor, then the conclusion is that some or all of the model is in error, and an improved model must be formulated. If the results match the field data, then the model may stand as a present best estimate of the sea's paleoceanography and possibly can be used to hindcast the nature of deposits formed in that

sea in areas with little or no field data. Either way, something new has been learned about nature.

This section is devoted to the derivation and exploration of a simple two-dimensional model of circulation in shallow seas, with an intended application to ancient epicontinental seas and coastal oceans. Epicontinental seas and coastal oceans are characterized by thin water columns on the order of tens to hundreds of meters, and horizontal distances on the order of hundreds of kilometers. They differ from the open ocean because coasts strongly constrain their motion and because surface effects that include wind shear stresses strongly influence a significant fraction of their water column. At the same time, much as in the open ocean, their motions are strongly affected by the Earth's rotation. The dominant motion of shallow oceans is rotary flow in which the current vector passes through 360° over roughly a day. Superimposed on this motion are residual and unidirectional flows at times scales of days to weeks. It is these latter flows that constitute "circulation" of a sea.

Circulation, in combination with wave-generated currents, is responsible for sediment dispersal and therefore plays a dominant role in sedimentation. To calculate actual three-dimensional coastal flows in their full vertical complexity is beyond the scope of this book, but it is possible to represent much of their behavior with respect to sediment transport by assuming a constant flow velocity over the vertical height of the water column, thereby simplifying this representation. Such a limitation is not as severe as first appears because for many coastal flows, steep velocity gradients develop only near the bed. This assumption simplifies the mathematics because depth-mean velocities may be used and the momentum equation in the vertical is reduced to the hydrostatic approximation. On the other hand, we must recognize that some important aspects of coastal flows will not be represented by such a model. For example, circulation near coastlines due to wind shear commonly produces bottom flows whose magnitude and direction contrast strongly with surface flows.

Derivation of the Model

If we agree to calculate only horizontal x- and y-directed, vertically averaged flow velocities, $U(x,y,t)$ and $V(x,y,t)$, and water surface elevation, $\zeta(x,y,t)$, we need only three equations for their solution. As usual, the three equations will come from the conservation of mass and momentum laws written for the two horizontal directions. The laws are applied to a block of water as pictured in Figure 5-18. The block, or cell, has a unit area of dx times dy and is $h+\zeta$ thick. First, consider conservation of water mass in the cell:

$$\text{Time rate of change of mass in cell} = \text{mass rate in} - \text{mass rate out} \qquad \textbf{(5-62)}$$

The first term, time rate of change of mass in the cell, can be written as:

$$\frac{\partial}{\partial t}\rho\,(h+\varsigma)\,dxdy \qquad \textbf{(5-63)}$$

In the second term in (5-62), mass can enter the cell in both the x and y directions. In the x direction the mass rate into the cell through the left face in Figure 5-18 is:

$$\rho U\,(h+\varsigma)\,dy \qquad \textbf{(5-64)}$$

As before, we use Taylor Series to define the mass flux out of the cell through the right face in Figure 5-18. The mass flux out that face is the mass flux into the cell in the x direction plus the rate at which that flux changes across the cell, or:

$$\rho U(h+\varsigma)\,dy + \frac{\partial}{\partial x}\rho U(h+\varsigma)\,dydx \tag{5-65}$$

Likewise, the mass flux into the cell through the front face is:

$$\rho V(h+\varsigma)\,dx \tag{5-66}$$

and the mass flux out through the back face is:

$$\rho V(h+\varsigma)\,dx + \frac{\partial}{\partial y}\rho V(h+\varsigma)\,dxdy \tag{5-67}$$

Substituting (5-63) through (5-67) into (5-62) and canceling common terms yields:

$$\frac{\partial}{\partial t}(h+\varsigma) = -\frac{\partial}{\partial x}U(h+\varsigma) - \frac{\partial}{\partial y}V(h+\varsigma) \tag{5-68}$$

The first term in (5-68) can be simplified by assuming that temporal changes in bed elevation are very small with respect to the other terms, in which case:

$$\frac{\partial \varsigma}{\partial t} + \frac{\partial}{\partial x}U(h+\varsigma) + \frac{\partial}{\partial y}V(h+\varsigma) = 0 \tag{5-69}$$

(5-69) is the continuity equation for two-dimensional, incompressible vertically averaged flow.

Next, consider the law of conservation of momentum, which states that:

Time rate of change of momentum in cell =
momentum flux in − momentum flux out +
sum of forces acting on fluid in the cell (5-70)

Because momentum is a vector quantity, this law must be applied in a particular direction. In the 2-D problem at hand, the law is applied in two directions, x and y in Figure 5-18. Considering the x direction first, we can write the left side of (5-70) as:

$$\frac{\partial}{\partial t}\rho\,(h+\varsigma)\,dxdyU \tag{5-71}$$

The first two terms on the right side of (5-70) represent the net momentum flux added to the cell. Momentum enters and exits the cell principally by convective momentum transfer. Convective momentum transfer occurs because water flowing into the cell possesses mass and is traveling at some velocity and therefore possesses momentum. X-directed momentum enters the cell by way of a mass flux through the left face which can be written as $\rho\,(h+\varsigma)\,dyU$. This mass entering per unit time has a velocity U and therefore brings momentum into the cell at

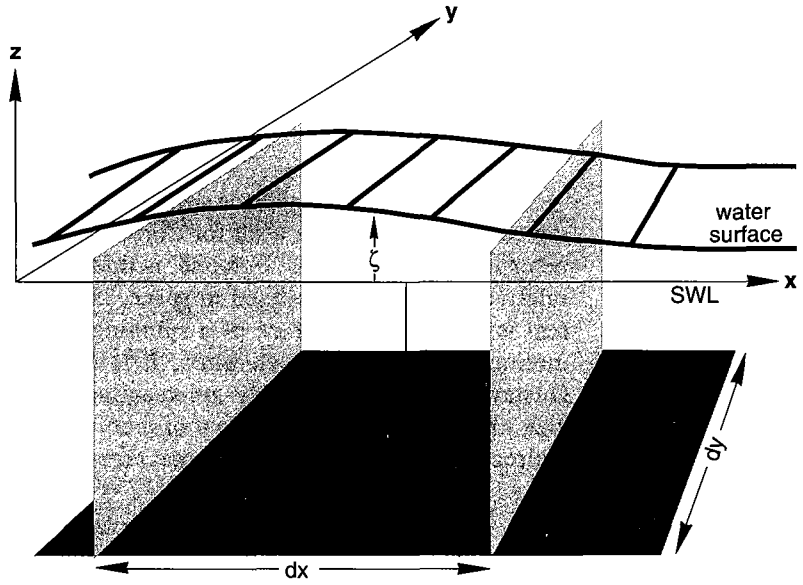

Figure 5-18 Diagram defining concepts and symbols used in equations for 2-D vertically averaged flow.

a rate of $\rho\,(h+\varsigma)\,dyUU$. This x-directed momentum exits the cell through the right face at a rate given by a Taylor series expansion, so that the net rate of addition of x-directed momentum through the two faces is:

$$\rho\,(h+\varsigma)\,dyUU - \left[\rho\,(h+\varsigma)\,dyUU + \frac{\partial}{\partial x}\rho\,(h+\varsigma)\,dyUUdx\right] = -\frac{\partial}{\partial x}\rho\,(h+\varsigma)\,dyUUdx \tag{5-72}$$

X-directed momentum also may enter the cell by way of a mass flux through the front face. That mass flux, represented by $\rho\,(h+\varsigma)\,dxV$, carries an x-directed momentum given by $\rho\,(h+\varsigma)\,dxVU$. The x-directed momentum exiting the back face per unit time is obtained by Taylor series as above, yielding a net rate of addition of x-directed momentum due to flow in the y direction of:

$$\frac{\partial}{\partial y}\rho\,(h+\varsigma)\,dxVUdy \tag{5-73}$$

The x-directed forces acting upon the fluid in the cell include the net pressure force, Coriolis force, and shearing forces at the bed and water surface. Consider the net pressure force first. The hydrostatic pressure acting on the left face in Figure 5-18 responsible for fluid motion is:

$$P = \rho g\varsigma \tag{5-74}$$

By Taylor series expansion the net x-directed pressure on the cell of fluid is:

$$\rho g\varsigma - (\rho g\varsigma + \frac{\partial}{\partial x}(\rho g\varsigma)\,dx) = -\rho g\frac{\partial \varsigma}{\partial x}dx \tag{5-75}$$

The net pressure force acting on the cell of fluid is the net pressure of (5-75) times the area over which it acts, or:

$$-\rho g\,(h+\varsigma)\,dy\frac{\partial \varsigma}{\partial x}dx \tag{5-76}$$

It is not immediately clear when applying Newton's general law of motion to the coastal ocean why a term for Coriolis force is needed. Why should not $\boldsymbol{F=ma}$ be enough? The answer, of course, is that $\boldsymbol{F=ma}$ applies only when $\boldsymbol{a}$ is measured relative to axes that are fixed in space, i.e., not accelerating. Our coordinate system is fixed on the surface of a spinning globe and therefore undergoes angular motion and constant acceleration. It is the Coriolis term, named after Gaspard Gustave de Coriolis, an early-nineteenth-century French engineer and mathematician, that adjusts the general law of motion to this rotating reference frame. In the x direction, the simplified horizontal component of the Coriolis force is:

$$C_x = 2\Omega\,(\sin\phi)\,V\,(h+\varsigma)\,\rho dxdy = fV\,(h+\varsigma)\,\rho dxdy \tag{5-77}$$

where: Ω = angular velocity of Earth's rotation (of magnitude 2π radians per sidereal day, or 7.29×10^{-5}rad s^{-1})

ϕ = angle of latitude.

If the bed and surface shear stresses are τ_o and τ_s, respectively, then the shearing forces are:

$$\tau_o dxdy + \tau_s dxdy \tag{5-78}$$

Substituting (5-71) through (5-73) and (5-76) through (5-78) in (5-70), canceling like terms, and expanding terms, yields:

$$U\frac{\partial}{\partial t}(h+\varsigma) + (h+\varsigma)\frac{\partial U}{\partial t} + U\frac{\partial}{\partial x}(h+\varsigma)\,U + (h+\varsigma)\,U\frac{\partial U}{\partial x} + U\frac{\partial}{\partial y}(h+\varsigma)\,V + (h+\varsigma)\,V\frac{\partial U}{\partial y} = fV\,(h+\varsigma) - g\,(h+\varsigma)\frac{\partial \varsigma}{\partial x} - \frac{\tau_o}{\rho} + \frac{\tau_s}{\rho} \tag{5-79}$$

Notice that by (5-69), the first, third, and fifth terms sum to 0 if we assume that temporal changes in bed elevation are negligible. Therefore, after dividing by $(h+\varsigma)$, (5-79) reduces to:

$$\frac{\partial U}{\partial t} + U\frac{\partial U}{\partial x} + V\frac{\partial U}{\partial y} = fV - g\frac{\partial \varsigma}{\partial x} - \frac{1}{\rho\,(h+\varsigma)}\,(\tau_{ox} - \tau_{sx}) \tag{5-80}$$

By a similar derivation the y-directed momentum equation may be found to be:

$$\frac{\partial V}{\partial t} + U\frac{\partial V}{\partial x} + V\frac{\partial V}{\partial y} = -fU - g\frac{\partial \varsigma}{\partial y} - \frac{1}{\rho\,(h+\varsigma)}\,(\tau_{oy} - \tau_{sy}) \tag{5-81}$$

Equations (5-69), (5-80), and (5-81) contain six unknowns, U, V, ζ, h, τ_o, and τ_s. These are reduced to three unknowns, U, V, and ζ, by appropriate boundary conditions. Still water depth h is specified for the particular bathymetry to be simulated. Bed shear stress τ_o is expressed in terms of depth mean velocity U or V, with the "law of the wall." This law expresses the time-averaged turbulent flow

velocity u as a function of distance from a wall z which in this case is the sea bed. It takes the form:

$$u = \frac{U_*}{\kappa} \log \frac{z}{z_o} \tag{5-82}$$

where: U_* = shear velocity,
κ = von Karman's constant (equal to 0.4 for clear water),
z_o = roughness length.

The depth mean velocity is defined as:

$$U = \frac{1}{(h+\varsigma)} \int_{-h}^{\varsigma} u dz \tag{5-83}$$

or substituting in (5-82):

$$U = \frac{U_*}{(h+\varsigma)\,\kappa} \int_{-h}^{\varsigma} \log \frac{z}{z_o} dz \tag{5-84}$$

Solving for τ_{ox}/ρ gives:

$$\frac{\tau_{ox}}{\rho} = \left(\frac{(h+\varsigma)\,\kappa}{\int_{-h}^{\varsigma} \log \frac{y}{y_o} dy} \right)^2 U^2 = \lambda U^2 \tag{5-85}$$

where: λ = nondimensional friction coefficient = $\frac{g}{C^2}$,
C = Chezy C.

In two dimensions, the equation becomes:

$$\frac{\tau_{ox}}{\rho} = \lambda U \sqrt{U^2 + V^2} \tag{5-86}$$

and

$$\frac{\tau_{oy}}{\rho} = \lambda V \sqrt{U^2 + V^2} \tag{5-87}$$

Surface shear stress due to wind is expressed by the quadratic forms:

$$\frac{\tau_{sx}}{\rho} = k W_x \sqrt{W_x^2 + W_y^2} \tag{5-88}$$

and

$$\frac{\tau_{sy}}{\rho} = kW_y\sqrt{W_x^2 + W_y^2} \qquad (5\text{-}89)$$

where: k = friction coefficient,
W = wind speed measured 10 m above sea surface,
ρ = water density.

As might be supposed, this equation set cannot be solved analytically, and as before we must turn to a numerical solution scheme.

Solution Scheme

The solution scheme, first presented by Koutitas (1988), is of finite difference type and chosen on the basis of its simplicity. The flow domain is discretized by a square horizontal grid of nodes Δx and Δy apart where $\Delta x = \Delta y$ (Figure 5-19). Water surface elevations, ζ, are computed at mesh centers, and U and V velocities are computed on alternate mesh sides. This geometry has the advantage that it economizes on the number of variables to be computed, being four times less than if all three variables were computed at each site. Nodes in the x direction occur at increasing distances from the origin at $i = 1\Delta x$ to $m\Delta x$ and in the y direction at $j = 1\Delta y$ to $n\Delta y$. U and V are calculated at times $n = 1\Delta t$ to $k\Delta t$ whereas ζ is calculated at $n = 1/2\Delta t$ to $(k+1/2)\Delta t$. In other words, at any timestep n, $\zeta^{n+1/2}$ is calculated first using the values of U^n and V^n, and is then used in the equations to

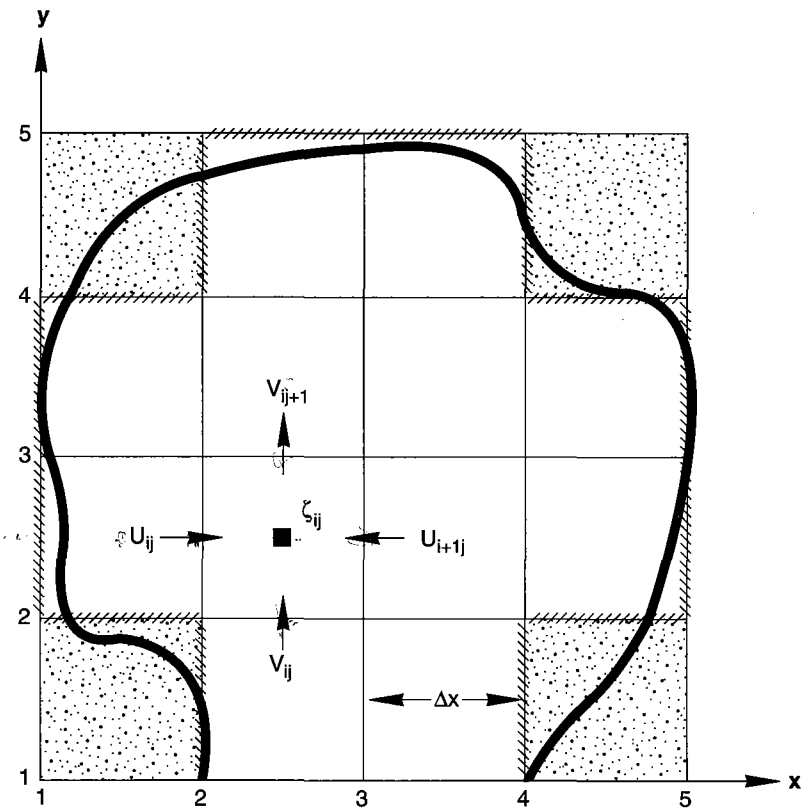

Figure 5-19 Discretization grid for 2-D circulation model.

calculate U^{n+1} and V^{n+1} (where the superscripts refer to timestep). This procedure leads to increased numerical stability.

The finite difference forms of (5-80), (5-81), and (5-69), are:

$$U_{ij}^{n+1} = U_{ij}^{n} - \frac{\Delta t}{8\Delta x}\left[(U_{i+1j}^{n} + U_{ij}^{n})^2 - (U_{ij}^{n} + U_{i-1j}^{n})^2\right] - \frac{\Delta t}{2\Delta y}\bar{V}_{ij}^{n}(U_{ij+1}^{n} - U_{ij-1}^{n}) - \frac{g\Delta t}{\Delta x}\left(\varsigma_{ij}^{n+\frac{1}{2}} - \varsigma_{i-1j}^{n+\frac{1}{2}}\right) - \frac{2g\Delta t U_{ij}^{n}\sqrt{(U_{ij}^{n^2} + \bar{V}_{ij}^{n^2})}}{C^2(h_{ij} + h_{i-1j})} + \Delta t f \bar{V}_{ij}^{n} \tag{5-90}$$

$$V_{ij}^{n+1} = V_{ij}^{n} - \frac{\Delta t}{8\Delta y}\left[(V_{ij+1}^{n} + V_{ij}^{n})^2 - (V_{ij}^{n} + V_{ij-1}^{n})^2\right] - \frac{\Delta t}{2\Delta x}\bar{U}_{ij}^{n}(V_{i+1j}^{n} - V_{i-1j}^{n}) - \frac{g\Delta t}{\Delta y}\left(\varsigma_{ij}^{n+\frac{1}{2}} - \varsigma_{ij-1}^{n+\frac{1}{2}}\right) - \frac{2g\Delta t V_{ij}^{n}\sqrt{(\bar{U}_{ij}^{n^2} + V_{ij}^{n^2})}}{C^2(h_{ij} + h_{ij-1})} - \Delta t f \bar{U}_{ij}^{n} \tag{5-91}$$

$$\varsigma_{ij}^{n+\frac{3}{2}} = \varsigma_{ij}^{n+\frac{1}{2}} - \frac{\Delta t}{2\Delta x}\left[U_{i+1,j}^{n+1}(h_{ij} + h_{i+1,j}) - U_{i,j}^{n+1}(h_{ij} + h_{i-1,j})\right] - \frac{\Delta t}{2\Delta y}\left[V_{i,j+1}^{n+1}(h_{ij} + h_{i,j+1}) - V_{i,j}^{n+1}(h_{ij} + h_{i,j-1})\right] \tag{5-92}$$

where:

$$\bar{V}_{ij}^{n} = \frac{(V_{i,j}^{n} + V_{i-1,j}^{n} + V_{i,j+1}^{n} + V_{i-1,j+1}^{n})}{4} \tag{5-93}$$

$$\bar{U}_{ij}^{n} = \frac{(U_{i,j}^{n} + U_{i,j-1}^{n} + U_{i+1,j}^{n} + U_{i+1,j-1}^{n})}{4} \tag{5-94}$$

As can be seen, this is an explicit finite-difference scheme. The values of the dependent variables at the new timestep can be computed directly from known values at the present timestep, thereby eliminating the need to solve a set of equations by matrix inversion. The penalty paid for this simplicity is a limitation in our choices of Δx and Δt. To preserve numerical stability, the Courant-Friedrichs-Lewy (CFL) criterion must be met:

$$\frac{\Delta t\sqrt{gh}}{\sqrt{2}\Delta x} < 1 \tag{5-95}$$

Remember that $\sqrt{gh}$ is the speed of a shallow water wave. This condition specifies then, that the timestep must be less than the time it takes for a wave to move between grid points. The $\sqrt{2}$ arises because waves travelling at 45° pass grid points at distances of $\sqrt{2}\Delta x$.

While it is clear how (5-90) through (5-92) can be applied to grid points in the computation field away from the coast, it remains for us to specify how to treat the solid and open boundaries of the computation domain. Just as in the one-dimensional cases discussed earlier, additional information, that is, boundary conditions, must be supplied to define the functions of integration. For coastal boundaries parallel to the x axis, the boundary condition is that $V_{ij}^n = 0$; for coastal boundaries parallel to the y axis, $U_{ij}^n = 0$. This is equivalent to assuming that the boundary is completely reflective, and while this is not strictly true, neither is it seriously in error. Along boundaries of the computation domain that are open to the sea, either the water surface elevation or velocities must be given through all time. Usually the water surface elevations are known, say from tidal stage gauges, and only techniques for specifying them will be pursued here. Either the total ς_{ij}^n time series at the boundary is known, or only the incident part of it, $\varsigma_{i_{ij}}^n = \varsigma_{ij}^n - \varsigma_{r_{ij}}^n$, where ζ_r is the elevation of the wave radiating seaward from within the computation domain (say from reflection off the coasts). Just as in the previous section, the elevation component of the radiated wave can be estimated from the theory of linear long waves:.

$$\frac{\partial \varsigma_r}{\partial t} + c\frac{\partial \varsigma_r}{\partial n} = 0 \qquad \textbf{(5-96)}$$

where: c = celerity of shallow water wave,

n = unit outward vector.

Likewise, the associated water velocities can be estimated from the conservation principle for a moving surge:

$$nU_n = \varsigma\sqrt{\frac{g}{h}} \qquad \textbf{(5-97)}$$

where: U_n is the velocity normal to the boundary.

Equations (5-90) through (5-97) and associated coastal boundary conditions have been formulated in a FORTRAN computer program (Program 20) following Koutitas (1988) to compute wind-driven and tidal flows in shallow seas of arbitrary geometry. The program first opens an input file named **INPUT.DAT** to read such constants as the time and space steps, friction coefficients, wind speeds in the x and y directions, Coriolis parameter, numbers of nodes in the x and y directions, number of time steps, number of boundary nodes for which boundary information is needed, timestep multiple at which dependent variables are to be printed out, and the amplitude and period of the incident waves (assumed to be of simple sine form).

Table 5-5
Values of *nb* defining various types of boundary nodes.

nb	boundary type
1	island
2	land to west
3	land to south
4	land to west and south
5	sea to west
6	sea to east
7	sea to north
8	sea to south
9	sea to west, land to south
10	sea to east, land to south
11	sea to north, land to west
12	sea to south, land to west

Next, the program reads the starting (*is*) and ending (*ie*) nodes of the computation field in the east-west direction, x, for each line in the north-south, y, direction. After that, the i and j numbers of the boundary nodes along the west and south sides of the grid are read along with an integer specifying the type of boundary as defined in Table 5-5. Next, the program assigns still-water depths to each node, calculates wind shear stresses, and sets all arrays to zero. The remainder of the program consists of a large loop that solves the equations for U, V, and ζ at each timestep, and prints values to their respective output files.

Some Examples

Experiment 5-5: Circulation in Response to Steady Wind

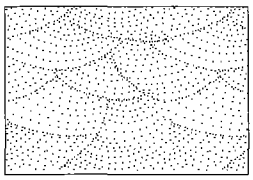

The first example demonstrates a temporally evolving nonuniform flow field in a rectangular coastal embayment driven by a steady, uniform wind (Figure 5-20). The embayment has been discretized into 625 cells, each 10 km on a side. The bathymetry consists of a seaward-sloping plane 6 m deep at the head, and 30 m deep at the entrance. A uniform wind stress of $W_x = W_y = 10$ m/s is applied to still water at $t = 0$. Other important variables are given in Table 5-6.

Table 5-6
Main data for Experiment 5-5.

Time step dt(s)	30
Space step dx(m) dy(m)	10000
Wind friction coeff. cs	5×10^{-6}
Chezy coeff. cf($m^{1/2}$ s^{-1})	0.01
Coriolis parameter f(s^{-1})	0.0001
Amplitude of incident long waves ampl(m)	0
Period of incident long waves (per s)	0

Figure 5-21 gives mesh diagrams of the water surface elevations and the vertically averaged velocity fields as they evolve. In response to the shear stress of the wind, water begins to flow towards the downwind corner of the basin, where it piles up. By timestep 400 (3.33 hours), flow velocities have increased from zero to a maximum 0.12 m/s and are parallel to the wind except near the coast. With time, the water surface deforms into a roughly uniformly sloping plane, 1.3 m above still water level at the downwind corner, and 0.3 m below sea level at the upwind corner (Figure 5-21b). Due to the sloping bed, flow velocities evolve toward a steady state pattern involving a clockwise circulation with inflow on the west and outflow on the east (Figure 5-21c). In regions where the U and V velocities and lateral gradients are small, the steady state geometry of the water surface is brought about by a balance between the wind shear on the water surface and the pressure gradient due to the sloping water surface. This is easily seen from (5-69), (5-80), and (5-81), which reduce to:

$$0 = -g\frac{\partial \varsigma}{\partial x} + \frac{1}{\rho\,(h+\varsigma)}\tau_{sx} \qquad \textbf{(5-98)}$$

$$0 = -g\frac{\partial \varsigma}{\partial y} + \frac{1}{\rho\,(h+\varsigma)}\tau_{sy} \qquad \textbf{(5-99)}$$

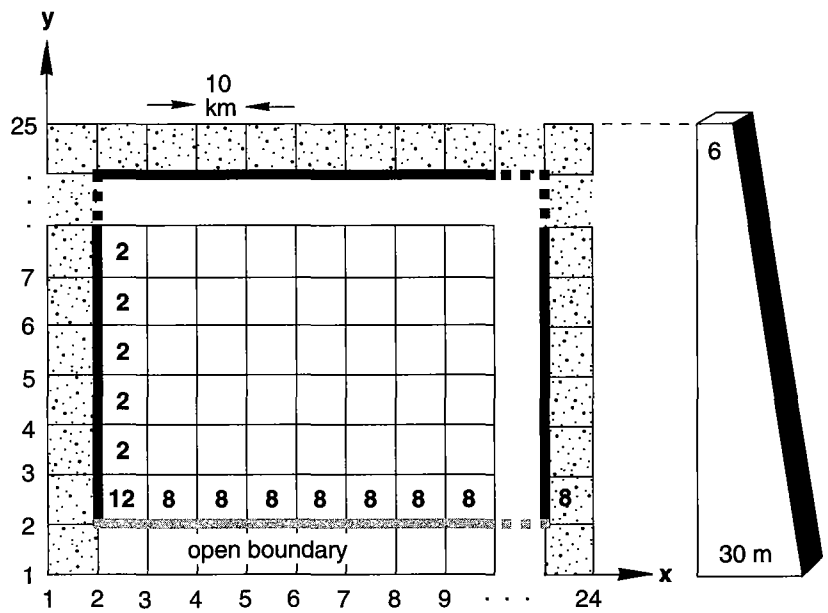

Figure 5-20 Geography and mesh for Experiment 5-5.

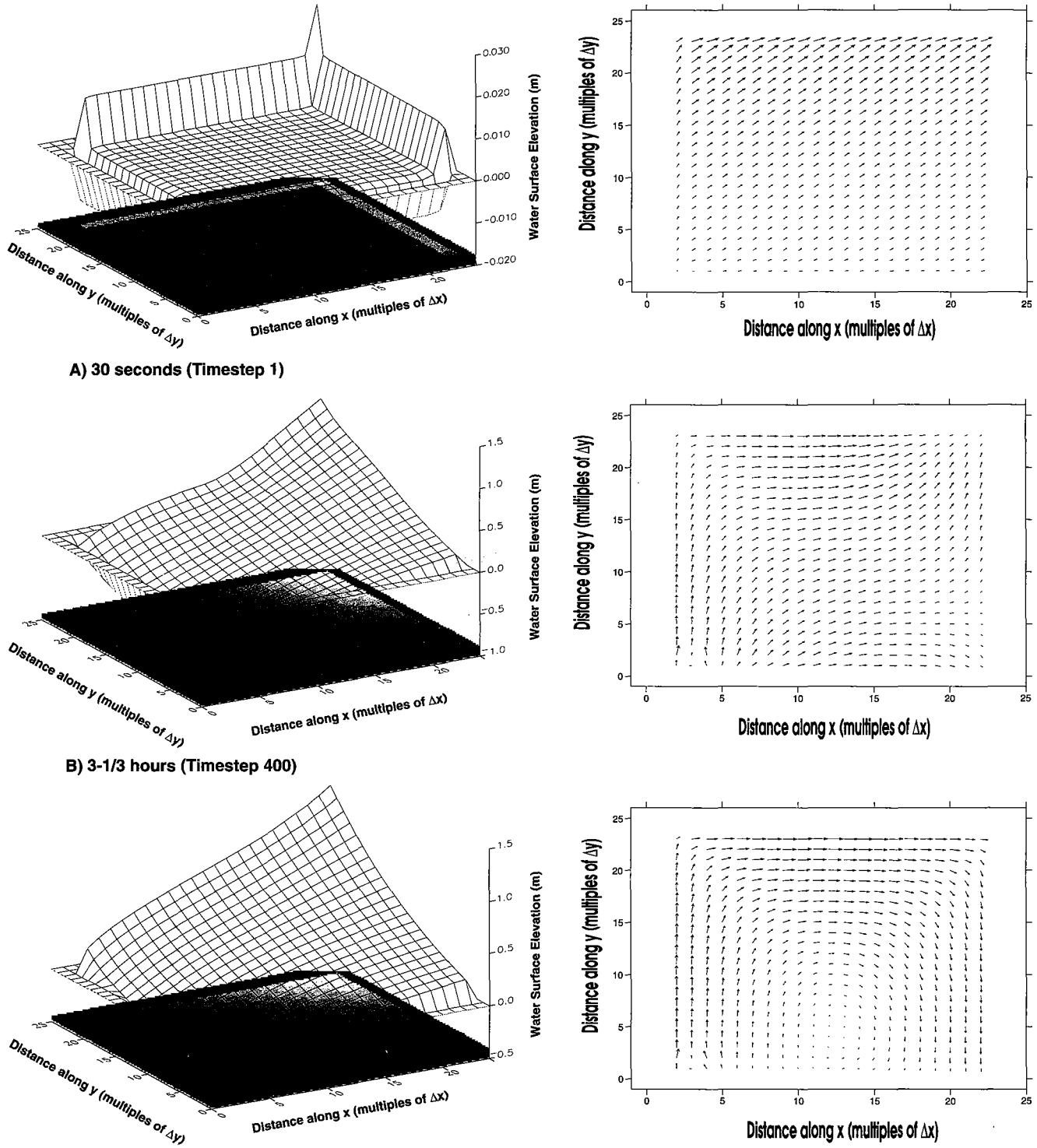

Figure 5-21 Water surface and circulation fields for Experiment 5-5 at timesteps: A) 1 (30 s), B) 400 (3.33 hours), and C) 2000 (16.67 hours).

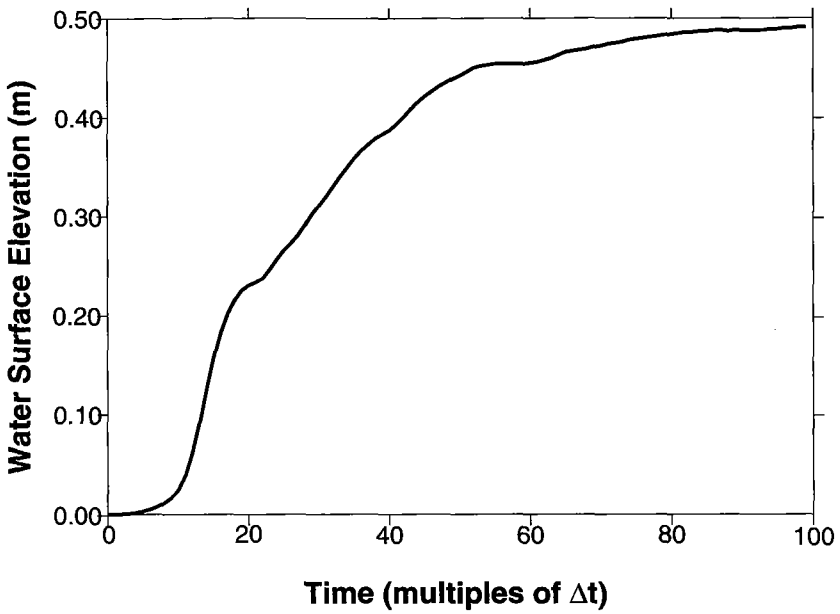

Figure 5-22 Water surface elevation through time at grid point (15,15) in Experiment 5-5.

These equations have the solution:

$$\varsigma = \frac{\tau_{sx}}{\rho g\,(h+\varsigma)}x + \frac{\tau_{sy}}{\rho g\,(h+\varsigma)}y \qquad \textbf{(5-100)}$$

showing that the water surface elevation is linearly proportional to the wind stress and location. In regions where U and V and their gradients are not zero, the force balance is between the pressure gradient and all the other terms in (5-80) and (5-81).

Close inspection of the water surface at timestep 400 reveals a series of subtle waves superimposed on the tilting surface. These are damped inertial oscillations called seiches, created by the sudden application of an impulse from the wind at $t = 0$. The seiches are best revealed by a plot of water surface elevation at a point through time (Figure 5-22). For those interested in their origin, Csanady (1982) gives a clear account. Thus we see that the response of a basin to a sudden wind is the development of wind setup and inertial oscillations of slowly decaying amplitude.

Experiment 5-6: Circulation in the Western Interior Seaway

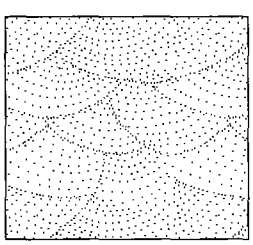

The Cretaceous Interior Seaway of North America was a large epicontinental sea which flooded a foreland basin east of the Cordilleran thrust belt (Figure 5-23). Fluctuations in eustatic sea level, tectonism, and climate caused the geography and bathymetry of the seaway to vary, sometimes producing a 1000-km-wide epeiric sea connecting the Boreal and Tethys Oceans, and at other times eliminating the seaway completely. Such large changes must have caused the circulation to vary widely, in turn varying sedimentary processes as well.

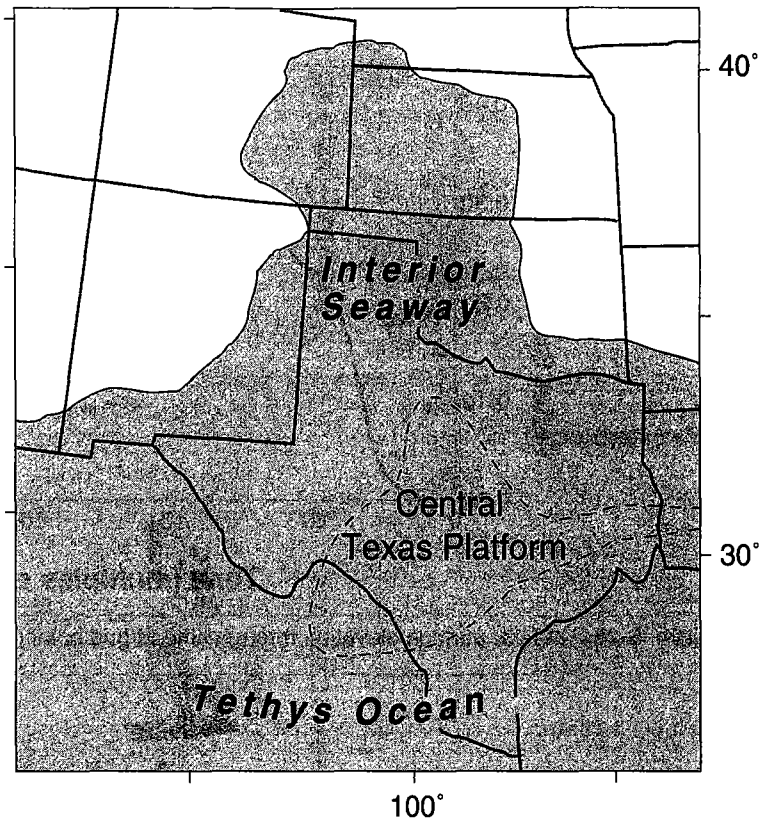

Figure 5-23 Cretaceous Interior Seaway of Western North America at an instant in Late Albian time (after Scott and Taylor, 1977).

Table 5-7
Main data for Experiment 5-6.

Time step dt(s)	7
Space step dx(m)	100000
Wind friction coeff. cs	5×10^{-6}
Chezy coeff. cf $(m^{1/2}\ s^{-1})$	0.01
Coriolis parameter f (s^{-1})	0.0001
Amplitude of incident long waves ampl(m)	1.0
Period of incident long waves per(s)	44640

In Experiment 5-6 we explore the tidal circulation that may have occurred during transgression of the Tethyian Ocean northward. The general dimensions of the seaway are based on estimates from outcrop studies, with detailed paleogeography and paleobathymetry ignored to simplify the interpretations. The paleogeography represented here (Figure 5-24) portrays an intermediate stage in the sea's transgression, with bathymetry consisting of a uniform slope from 64 m to 400 m south. An incoming tidal wave of M_2 type, with a period of 12.4 hours (44,640 s) and amplitude of 1 m, was applied at the southern boundary. Other parameters are given in Table 5-7 and Table 5-8.

Results (Figure 5-25) are plotted every 1000 timesteps (1.94 hours) for a 17.5-hour period, starting at the time of high water of the incident wave (timestep 10000). Notice that the tidal wave crest sweeps counterclockwise around the margin of the seaway, exiting to the Tethyian Ocean on the western side of the entrance. The crest is highest along the coast and decreases into the center of the seaway. These are classic Kelvin waves, topographically trapped along the coast by the Coriolis force. The tidal ranges around the basin (Figure 5-25) are higher along the eastern margin compared with the western margin due to frictional

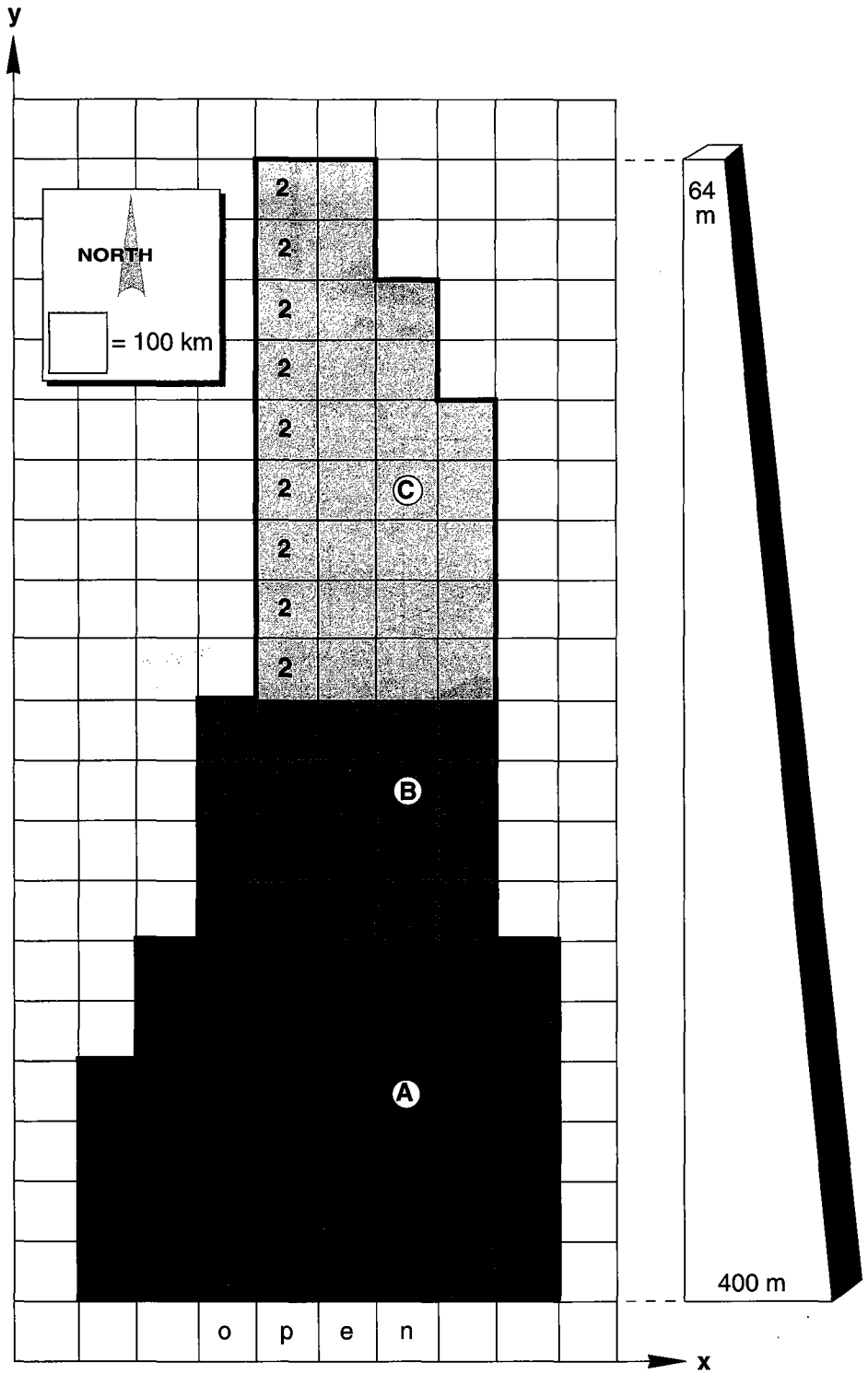

Figure 5-24 Finite-difference grid for Experiment 5-6, simulating southern entrance to Cretaceous Western Interior Seaway of North America.

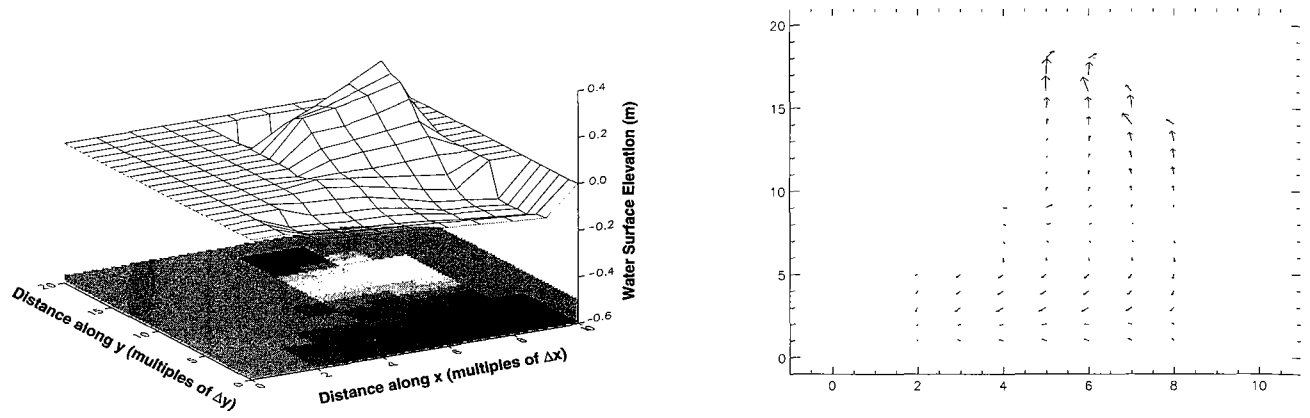

1.94 hours

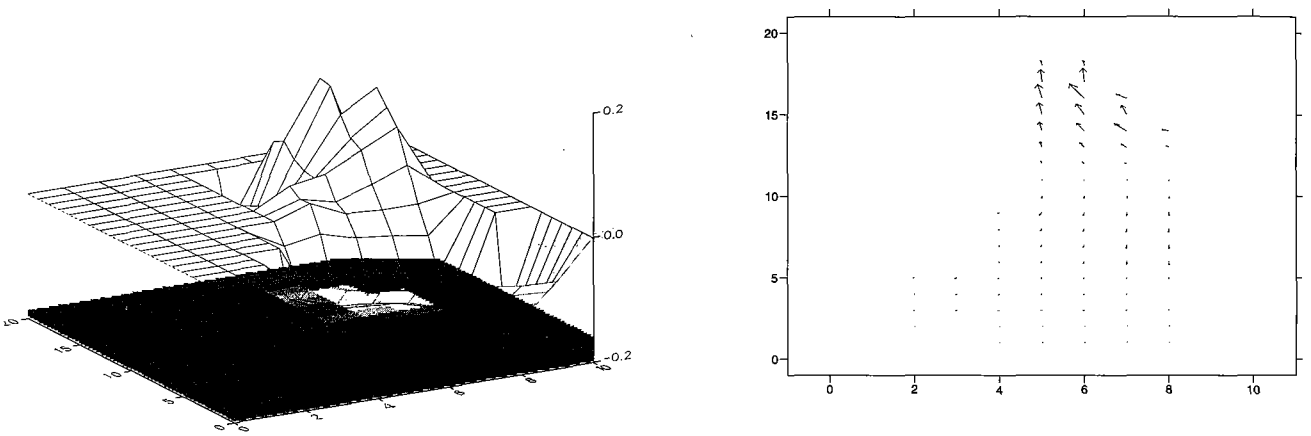

3.88 hours

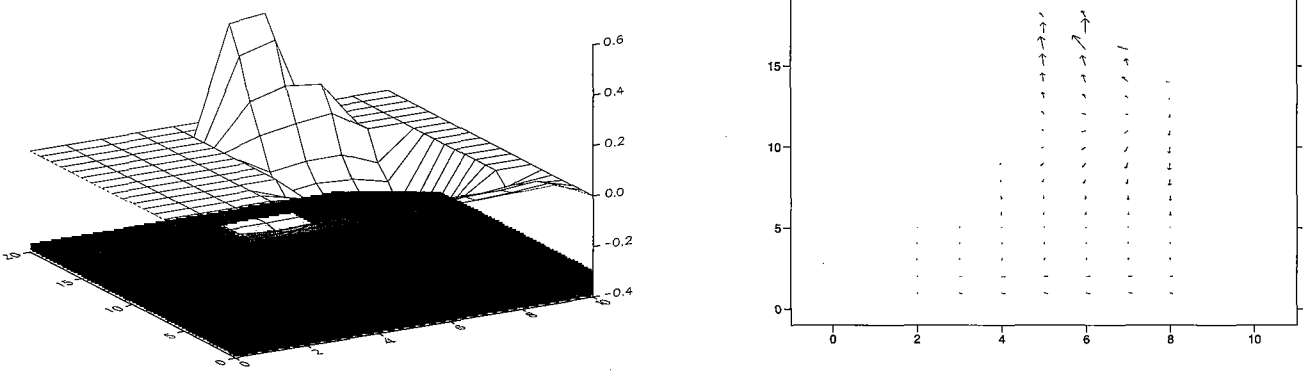

5.82 hours

Figure 5-25 Results for Experiment 5-6 plotted every 1000 timesteps (1.94 hours) for a 17.5-hour period of incident wave. Perspective diagrams show water surface elevation and maps show velocity vectors.

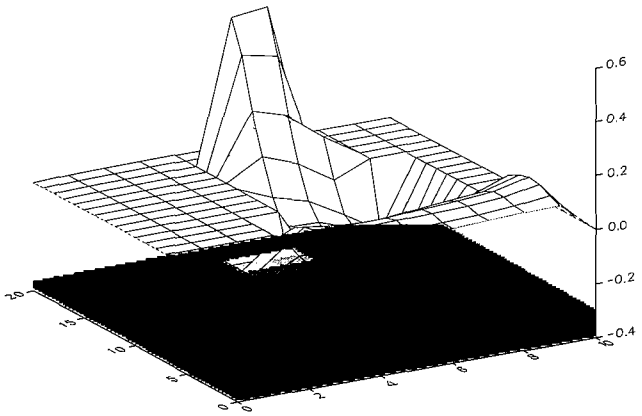

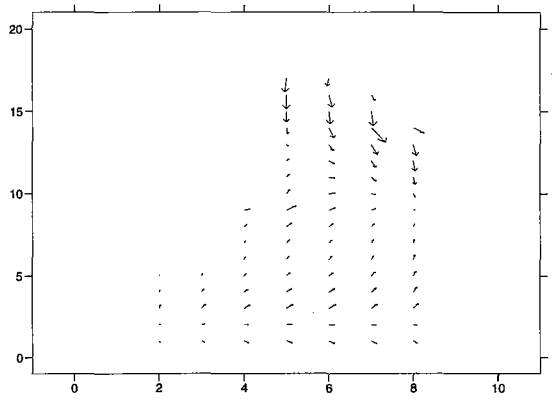

7.76 hours

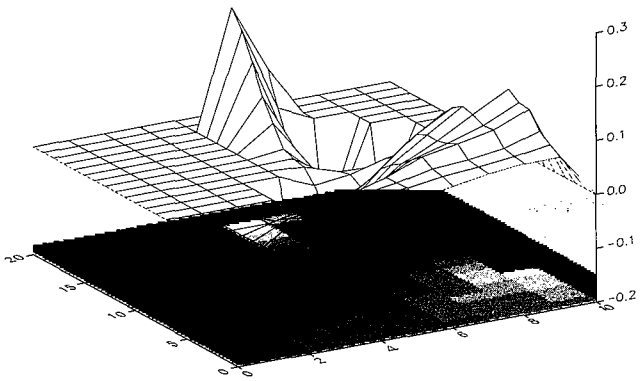

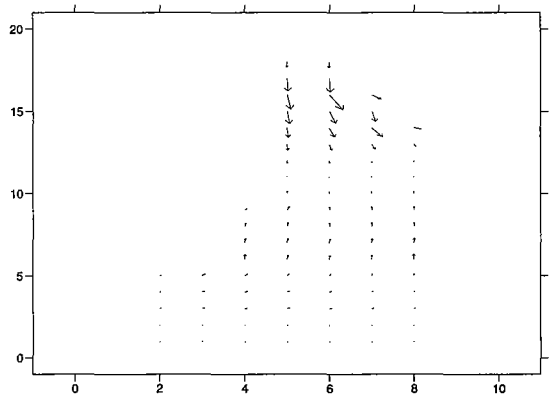

9.70 hours

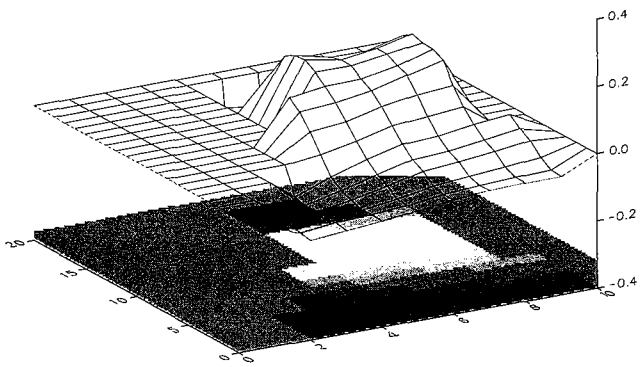

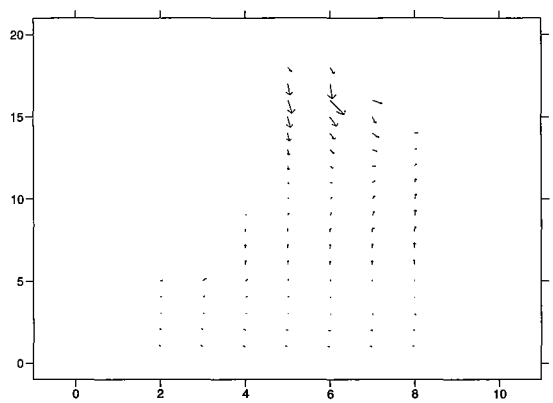

11.64 hours

Figure 5-25 continued

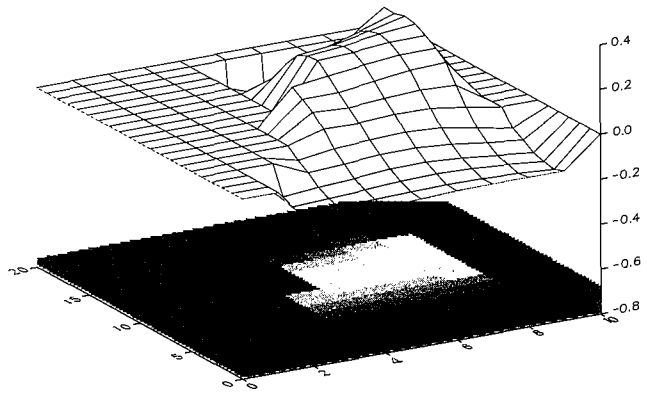

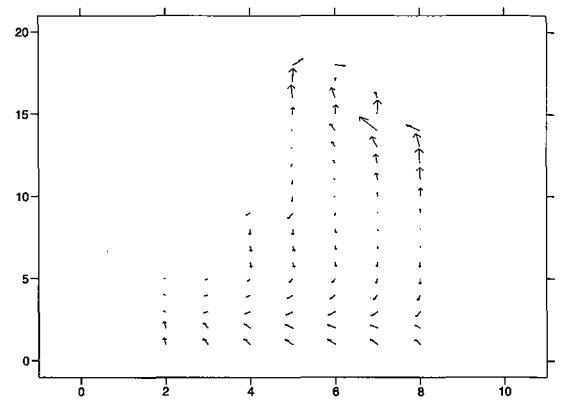

13.58 hours

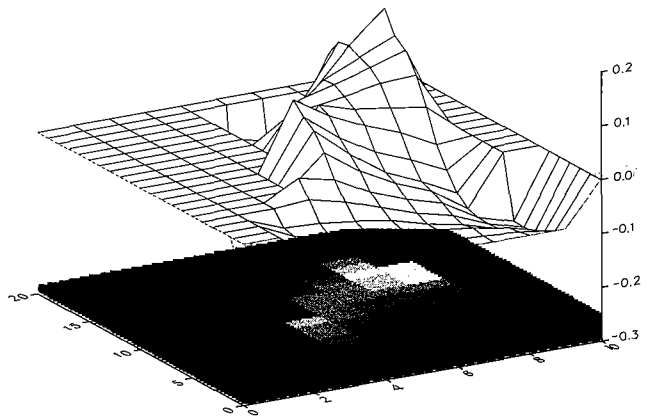

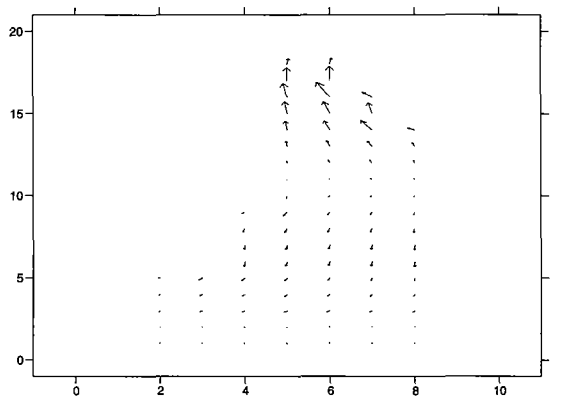

15.52 hours

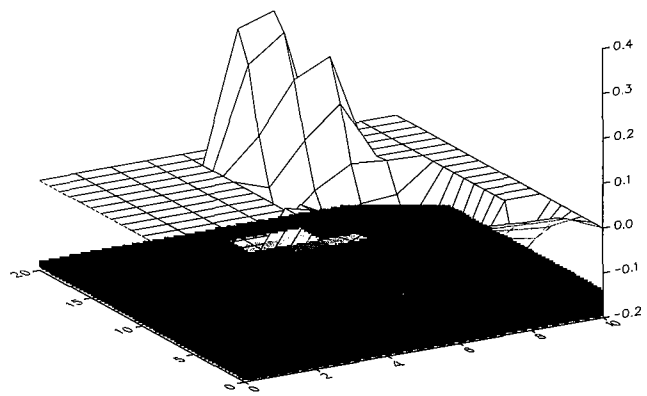

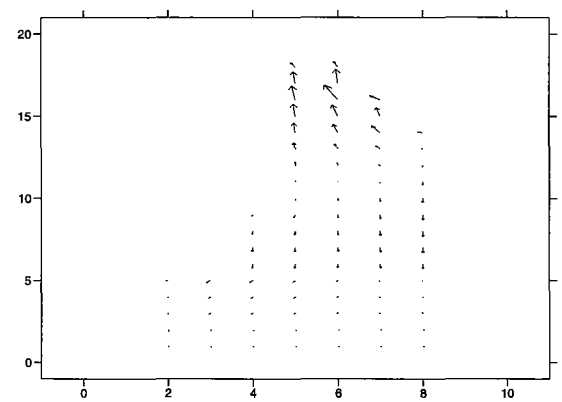

17.46 hours

Figure 5-25 continued.

losses. The closest modern example is the tide of the North Sea, which enters from the north, tracks south along the east coast of Britain, crosses the straights of Dover, and travels north along the coasts of the Netherlands and Germany, all the while decreasing in height.

Notice also that the ranges exhibit two lows and are highest at the head of the embayment (about 1.5 m). This reflects a standing wave system superimposed on the progressive Kelvin wave. The reason for this standing wave is that the two waves traveling in opposite directions interfere with one another. The high ranges at the head are a result of convergence effects, as discussed earlier in this chapter, and constructive interference of the inbound and outbound waves [see Pond and Pickard (1983) for more on tidal resonance].

Thus we conclude that the tides in the southern limb of the Western Interior Seaway acted as a mixture of progressive Kelvin waves and standing waves. The highest tidal ranges, and therefore the greatest probability for tidal environments (all other factors being equal), would be at the head of the embayment and along the southeastern coast.

Table 5-8
Input file INPUT.DAT for Experiment 5-6

```
7.0 100000.0 0.000005 0.01 0.0
0.0 0.0001 10 22 24000 26
100.0 1.0 44640.0
      \dt,dx,cs,cf,wx,wy,f,
im,jm,nm,kb,dat,ampl,per
2 9     \is(j),ie(j)
2 9
2 9
2 9
2 9
3 9
3 9
4 8
4 8
4 8
4 8
5 8
5 8
5 8
5 8
5 8
5 7
5 7
5 6
5 6
5 6
2 2
12
\ib(k),jb(k),nb(k)
2 3 2
2 4 2
2 5 2
3 6 2
3 7 2
4 8 2
4 9 2
4 10 2
4 11 2
5 12 2
5 13 2
5 14 2
5 15 2
5 16 2
5 17 2
5 18 2
5 19 2
5 20 2
3 2 8
4 2 8
5 2 8
6 2 8
7 2 8
8 2 8
9 2 8
```

WIND-GENERATED WATER SURFACE WAVES

The drag of the wind over water creates water surface waves, which in the area where waves are generated are called *seas*, and out of the generating area are called *swell.* Because gravity is the restoring force, these are also called gravity waves. If the distribution of ocean surface wave energy is plotted over the whole frequency band from 10^{-6} to 10^{2} cycles per second, it is clear that gravity waves with frequencies in the range 1/5 to 1/15 (that is, with periods of from 5 to 15 seconds) contain most of the ocean's surface wave energy. It should come as no surprise that waves are very important in shaping coastlines and transporting sediment on shallow marine shelves.

In this section, we start with a general description of gravity waves. To keep the discussion simple, the usual assumptions will be made: (1) the waves can be considered as small perturbations of a fluid otherwise at rest; (2) fluid density is constant; (3) the fluid is inviscid (lacks viscosity); (4) the seabed is nearly horizontal (slope less than 1 on 10) and impermeable; (5) the waves are plane and long-crested, and (6) Coriolis effects and surface tension can be neglected. These assumptions allow the derivation of small-amplitude, or linear wave, theory, first obtained by Sir George Biddell Airy in 1845. Sir George was Lucasian Professor of Mathematics at Cambridge and the seventh Astronomer Royal.

Next, we will present some empirical functions which predict the wave field arising under a cyclonic wind field. This requires first deriving the cyclonic wind field model, and then the wave field model. Of course, more sophisticated wave prediction models exist, but these are beyond the scope of this book. After wave generation, we treat wave transformation. It is well known that waves change their speed, direction, wavelength, and height as they travel over a submerged topography. Predicting a wave field and its effect on bed sediment therefore requires a model of wave shoaling and refraction. Finally, we consider sediment transport under a combined oscillatory-unidirectional flow.

Simple Periodic, Progressive, Linear Waves

Simple periodic waves in a particular water depth can be characterized by the displacement of the water surface, wavelength, amplitude, period, and speed of forward

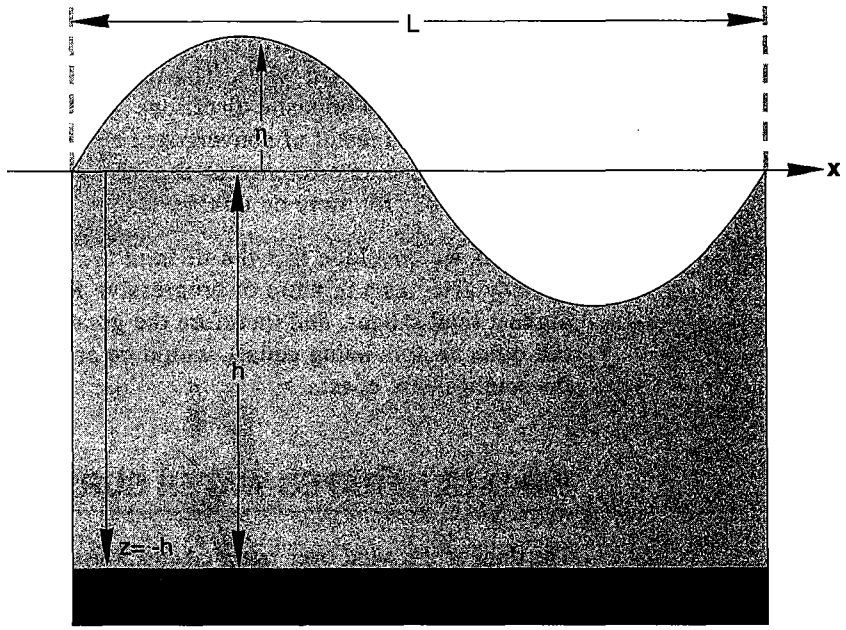

Figure 5-26 Definition sketch for simple progressive waves.

propagation, also called celerity, as functions of x and t (Figure 5-26). Wave theory defines the functional relationships among these variables. Airy wave theory accomplishes this task by using the continuity of mass equation, Bernoulli's equation, and a constraint that the solutions should be simple harmonic functions in time. If you remember from (5-8), the continuity equation written for the region $-h < z < \eta$ in Figure 5-26 would be:

$$\frac{\partial u}{\partial x} + \frac{\partial w}{\partial z} = 0 \tag{5-101}$$

Airy, following the method of Laplace, then postulated the existence of a function $\Phi(x,z,t)$, called the *velocity potential*, which satisfied the mathematical conditions that:

$$u = -\frac{\partial \Phi}{\partial x} \quad \text{and} \quad w = -\frac{\partial \Phi}{\partial z} \tag{5-102}$$

Substituting (5-102) into (5-101) yields the Laplace equation:

$$\frac{\partial^2 \Phi}{\partial x^2} + \frac{\partial^2 \Phi}{\partial z^2} = 0 \tag{5-103}$$

The Laplace equation is used frequently in studies of heat, sound, light, and hydrodynamics, as might be expected for an equation describing conservation of a property.

Two boundary conditions are needed to solve (5-103), one at the bed and one at the water surface. Airy assumed that no flow would occur into or out of the bed and therefore he wrote the bottom boundary condition as:

$$w = -\frac{\partial \Phi}{\partial z} = 0 \quad \text{on } z = -h \tag{5-104}$$

To obtain the boundary condition at the water surface, Airy used Bernoulli's equation, which you might remember from Chapter 4. Here it is written for two dimensions and unsteady flow:

$$-\frac{\partial \Phi}{\partial t} + \frac{1}{2}(u^2 + w^2) + \frac{p}{\rho} + gz = 0 \tag{5-105}$$

where: a = velocity potential,
u and w = x- and z-directed fluid velocities,
p = fluid pressure,
ρ = fluid density,
g = gravitational acceleration.

Airy assumed that the velocity terms in (5-105) are small with respect to the other terms. By definition, the fluid pressure at $z = \eta$ is zero, thereby leading to:

$$\eta = \frac{1}{g}\frac{\partial \Phi}{\partial t} \quad \text{on } z = \eta \tag{5-106}$$

To make (5-106) readily usable, Airy assumed that the waves were small enough that satisfying the boundary condition at $z = 0$ is approximately equivalent to satisfying it at $z = \eta$, yielding:

$$\eta = \frac{1}{g}\frac{\partial \Phi}{\partial t} \quad \text{on } z = 0 \tag{5-107}$$

Airy solved (5-103), (5-104), and (5-107) for the velocity potential, Φ, obtaining:

$$\Phi = -\frac{ag\cosh k(h+z)}{\sigma \cosh kh}\cos(kx - \sigma t) \tag{5-108}$$

where: a = wave amplitude,
g = gravitational acceleration,
cosh = hyperbolic cosine,
k = wave number, equal to $2\pi/L$,
h = water depth,
z and x = locations as defined in Figure 5-26,
σ = wave angular frequency, equal to $2\pi/T$,
t = time.

All of the functional relationships among a wave's wavelength, period, celerity, water depth, and so on are obtainable from (5-108). For example, to obtain

Table 5-9 Relationships predicted by Airy wave theory

Parameter	General Expression
Surface elevation, $\eta(x,t)$	$\eta = \frac{H}{2}\cos(kx - \sigma t)$
Phase velocity, C	$C = \frac{gT}{2\pi}\tanh\left(\frac{2\pi h}{L}\right)$
Wavelength, L	$L = \frac{gT^2}{2\pi}\tanh\left(\frac{2\pi h}{L}\right)$
Horizontal orbital diameter, d	$d = H\frac{\cosh[k(z_o + h)]}{\sinh(kh)}$
Horizontal orbital velocity, u	$u = \frac{\pi H \cosh[k(z+h)]}{T\sinh(kh)}\cos(kx - \sigma t)$

$\eta(x,t)$, one substitutes (5-108) into (5-107) and differentiates with respect to time after setting z equal to zero. The result is given in Table 5-9 along with other important relationships.

Reflection on the general expressions in Table 5-9 should convince you that two end members of simpler solutions exist, one for deep water where $h/L > 1/2$, and one for shallow water where $h/L < 1/25$. For example, in deep water, $\tanh(2\pi h/L)$ approaches unity and wave celerity reduces to $C = gT/2\pi$.

In subsequent discussions it will be important to determine how wave characteristics such as wavelength and celerity vary as a wave travels into shallower water. This task is greatly simplified by a fact of some consequence: *the wave period is independent of the depth for a simple harmonic wave train.*

Predicting Waves from a Wind Field

Predicting a wave field from a wind field is a burdensome business. The mechanisms of wave generation by wind are not completely understood, and the processes of energy gain, transfer among wave frequencies, and dissipation by breaking and bottom friction are numerous. To make matters worse, in areas of geometrically complex winds, the wave field may consist of waves of varying heights and frequencies traveling in directions that box the compass. It is not surprising, then, that numerical codes for waves used by the superpower navies run to tens of thousands of lines.

As we have seen before, however, simpler prediction schemes are available if we sacrifice some accuracy and generality. In wave prediction, these schemes rely

upon empirical relationships between the dependent variables of wave energy or height, wave period, and wave direction as functions of the independent variables, wind speed, duration, fetch, and water depth, where fetch is defined as the region over which the wind shear is applied to the water surface. The approach presented here is limited to calculating wave conditions due to hurricanes. We think the bulk of shallow marine sediment is distributed around sedimentary basins during cyclonic storms such as hurricanes and typhoons because sediment transport is proportional to a high power of bottom flow velocity. Fair weather processes may occur most of the time, but they accomplish little sediment transport.

We first calculate a cyclonic wind field, and then calculate the wave field under it, using equations derived by the U.S. Army Corps of Engineers at their Coastal Engineering Research Center in Vicksburg, Mississippi.

Predicting the Wind Field for Cyclones

In the circulation model presented earlier in this chapter, it was necessary to specify the wind velocity at each node in the computation field as a boundary condition. We could do the same to compute the cyclonic wave field, but this method of setting the wind boundary condition is not particularly useful if we want to simulate storms where the wind fields are elliptical. Here we present a mathematical model of a hurricane's surface wind field. The model is due to V. A. Myers as described by Harris (1958) and presented in the *Shore Protection Manual* (Anonymous, 1984). The gradient wind speed at a radial distance r from the storm center in SI units is:

$$\frac{U_{gr}^2}{r} + fU_{gr} = \frac{1}{\rho_a}(p_n - p_o)\frac{R}{r^2}e^{-\frac{R}{r}} \qquad \textbf{(5-109)}$$

where: f = Coriolis parameter,
ρ_a = air density,
p_n = pressure at outskirts of storm,
p_o = central pressure,
R = radial distance from storm center to region of maximum wind speed.

The wind speed calculated in (5-109) is called the gradient wind speed because it is due to the pressure gradient alone. If the storm is moving forward, then a correction term is needed, because windspeeds to the right of a storm track (in the northern hemisphere) are always observed to be higher than those on the left. Simple vector addition will not do, because the effect of storm motion on the wind field seems to decrease with distance from R. One correction term in common use is:

$$U_{SM}(r) = \frac{Rr}{R^2 + r^2}V_F \qquad \textbf{(5-110)}$$

where: $U_{SM}(r)$=term added vectorially to wind velocity at each value of r,
V_F=velocity of storm center.

These equations have been coded in Program 21 along with input-output statements, to provide a module for driving water circulation and wave generation.

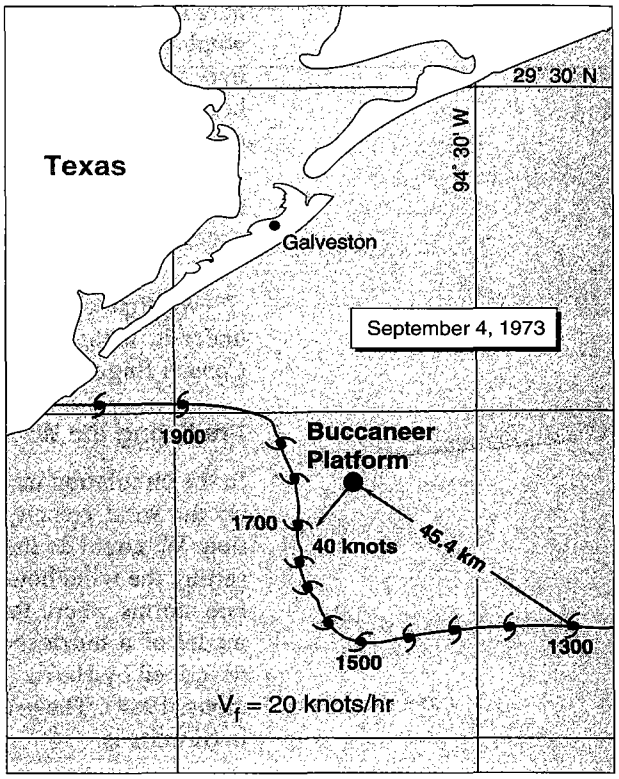

Figure 5-27
Detailed storm track for Tropical Storm Delia near Buccaneer platform on September 4, 1973.

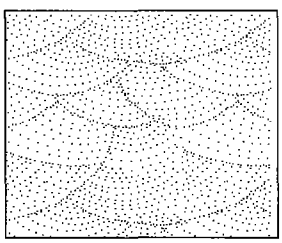

Experiment 5-7: Calculating the Wind Field under Tropical Storm Delia

As an example of the wind field created by the above algorithm, consider Delia, a tropical storm which came ashore near Galveston, Texas, in September 1973 (Figure 5-27). Delia passed over an oil drilling platform named Buccaneer, located in 20 m of water off Galveston, where a wind gauge recorded its passage. The wind speed recorded at Buccaneer on September 4, 1973 at 1300 hours was 40 knots (18 m/s). The computed wind speed is obtained using the recorded pressure differential, storm speed, and other variables at 1300 hours as given in Table 5-10. The computed winds show the characteristic hurricane pattern, with higher winds to

Table 5-10 Experiment 5-7 input file for computation of Tropical Storm Delia's wind field

1 25 25 10000.0 10000.0	**/LMAX,IM,JM,DX,DY**
12 12 2	**/MCENT,NCENT,LSC**
5.6 180.0 99800.0 101200.0 64400.0 3000000.0 0.	**\SVEL,SDIR,PCENT,PEDGE,RMAXW,SRAD,DEFCON**

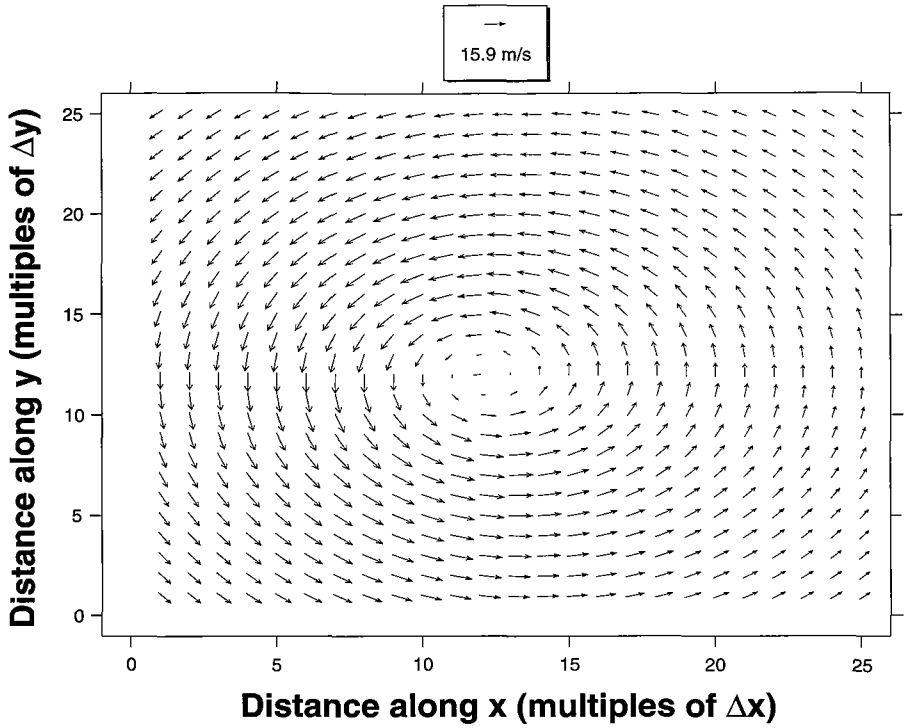

Figure 5-28 Experiment 5-7 computed wind field for Tropical Storm Delia at 1300 hours on September 4, 1973, as it moves almost due west. Magnitude of vector at node (14,1) south-southeast of the eye is 15.9 m/s.

the right of the storm when viewed down the stormtrack (Figure 5-28). The computed wind speed at Buccaneer is 20 m/s, which compares favorably with the observed of 18 m/s.

Predicting the Wave Field for Cyclones

Now that the cyclonic wind field is known, it would seem simple to predict the wave field. We might use any of the published relationships between wave characteristics of the fully developed sea and wind speed, duration, and fetch. The problem arises, however, that the large changes in wind speed, fetch, and duration under a cyclone do not allow a fully arisen sea state to develop. Furthermore, the wave field at any particular site will consist of a locally generated sea and a swell from other parts of the storm. Our solution is to use an empirical model derived by the U.S. Army Corps of Engineers (Anonymous, 1984).

The equations presented below predict the deep-water significant wave height and period at the point of maximum wind in a slowly moving hurricane. Significant wave height $H_{1/3}$ is defined as *the average height of the one-third highest waves.* Significant wave period is approximately the average period of 10 to 15 successive prominent waves. As noted above, the point of maximum wind occurs to the right of a storm moving away from an observer in the northern hemisphere.

The equations are:

$$H_{o1/3} = 5.03e^{\frac{R\Delta p}{4700}}\left[1 + \frac{0.29\alpha V_F}{\sqrt{U_R}}\right] \quad \textbf{(5-111)}$$

$$T_s = 8.6e^{\frac{R\Delta p}{9400}}\left[1 + \frac{0.145\alpha V_F}{\sqrt{U_R}}\right] \quad \textbf{(5-112)}$$

$$U_R = 0.865U_{max} + \frac{1}{2}V_F \quad \textbf{(5-113)}$$

where: $H_{o1/3}$ = deep water significant wave height in meters,

T_s = corresponding significant wave period in seconds,

R = radius of maximum wind in kilometers,

Δp = normal pressure (760 mm of mercury) minus central pressure of hurricane in mm of mercury,

α = coefficient depending upon forward speed of the hurricane; for slowly moving hurricane, $\alpha = 1.0$,

V_F = forward speed of hurricane in meters per second,

U_R = maximum sustained windspeed in meters per second, calculated for 10 meters above mean sea surface at radius R, and

U_{max} = maximum gradient wind speed 10 meters above water surface calculated from (5-109) and (5-110) when $r = R$.

Note that these equations are a dimensional mixture; millimeters of mercury, kilometers, and meters are all combined, but Δp in Pascals is converted to Δp in millimeters of mercury when multiplied by 7.5×10^{-3}.

Equations (5-111) through (5-113) give us the wave height and period at one point under the storm. The wave characteristics at other points are found by reducing these values according to two empirical functions determined by the Coastal Engineering Research Center of the Army Corps of Engineers (Anonymous, 1984). Figure 5-29 presents isolines of significant wave height relative to the maximum value at the point of maximum wind. Wave periods are calculated from an empirical equation:

$$T = 12.1\sqrt{\frac{H_o}{g}} \quad \textbf{(5-114)}$$

The wave directions are wind directions computed in the previous section. These relationships are coded in FORTRAN in Program 22.

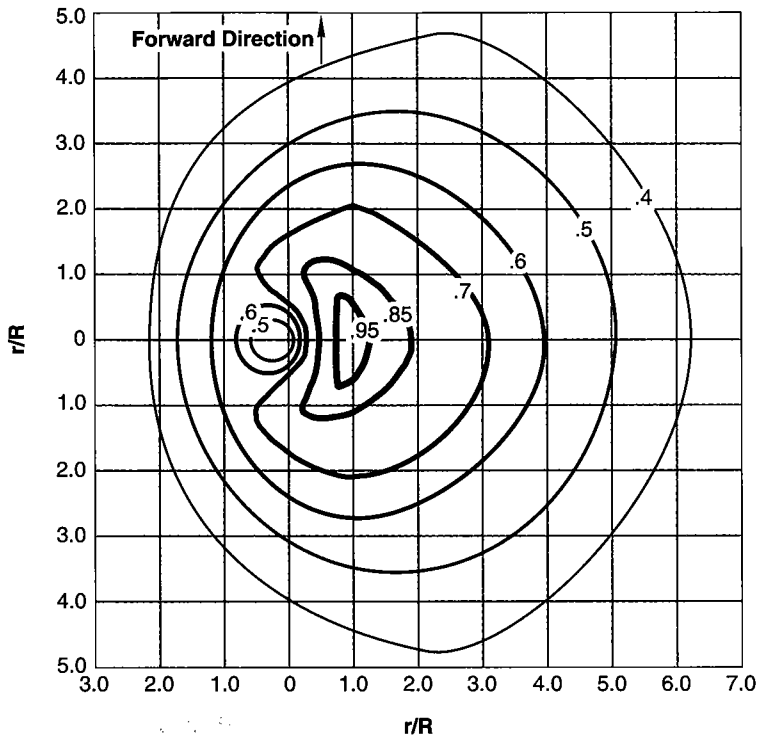

Figure 5-29 Isolines of relative significant wave height for slow-moving hurricane. Relative wave height is the ratio of wave height to maximum wave height. r = radius of interest; R = radius of maximum wind. Origin marks eye of storm traveling north (Anonymous, 1984).

Experiment 5-8: Calculating the Wave Field Under Tropical Storm Delia

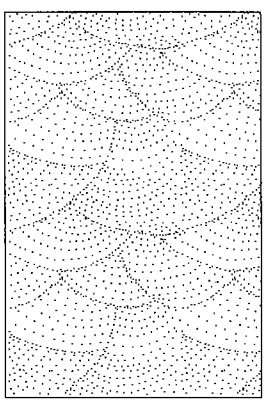

As described above, Tropical Storm Delia passed near an oil drilling platform, where in addition to meteorological instruments, a wave staff and three electromagnetic current meters had been installed, thanks to G. Z. Forristall and colleagues of Shell Development Company (Forristall, Hamilton, and Cardone, 1977; Forristall, Ward, Cardone, and Borgmann, 1978). The observed wave field during the passage of Delia (Figure 5-30) consisted of 2.9 m waves at 0600 hours on September 4, 1973, that increased to 4.9 m waves at 1300 hours, and then rapidly decreased to 2.4 m waves after 1800 hours. Figure 5-27 shows that at 1300 hours the storm's eye was about 45 km southeast of the platform and was heading due west. The radius of maximum winds for Delia was about 64 km. Thus, from 0600 hours to 1300 hours, the seas around Buccaneer Platform were subjected to increasingly higher wind speeds to the right of the storm as viewed down its track. From 1300 to 2400 hours wind speeds decreased as the eye moved within 10 km of the platform. Although it would be easy to simulate the temporal evolution of the wave field, we will leave an exercise of that type to the reader. Here, we will predict the significant wave height at 1300 hours.

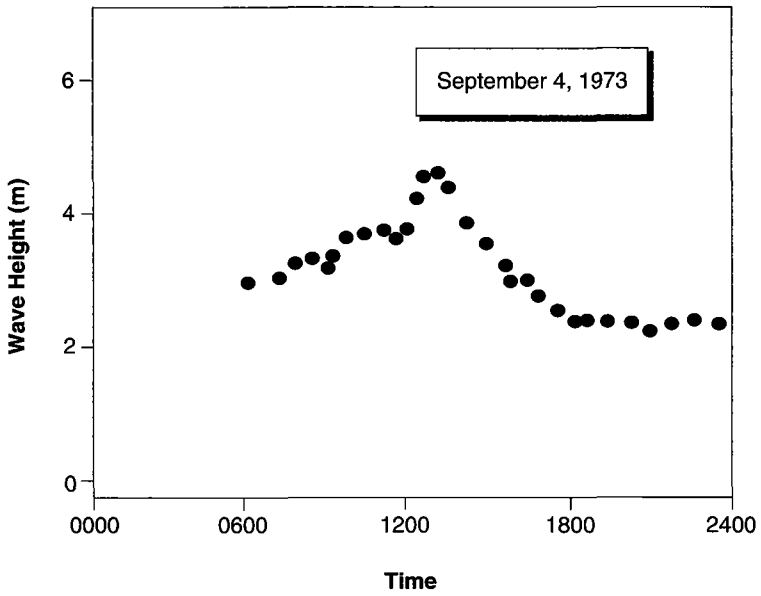

Figure 5-30
Significant wave height at Buccaneer platform during the passage of Tropical Storm Delia. See Figure 5-27 for location of platform with respect to storm track.

Table 5-11 Experiment 5-8 input data file simulating the wave field under Tropical Storm Delia at 1300 hours on September 4, 1973.

```
18.1 64400.0 23.0 5.6 25 25 10000.0 10000.0 120000.0 120000.0 180.0
    \Umax,R,deltap,Vsubf,im,jm,dx,dy,xo,yo,sdir
```

The input data are contained in Table 5-11, and a contour plot of computed significant wave heights is contained in Figure 5-31. The computed significant wave height is near that observed. The computed significant wave period obtained with (5-114) is about 9.5 seconds

Wave Transformations

The reader may have noticed that the wind-sea model discussed above predicts *deep water* significant wave characteristics. The sedimentary geologist wants to know how these waves will interact with the bed, and therefore must know their shallow water characteristics. Inspection of relationships in Table 5-9 will show that waves are transformed as they travel into shallower water. Their wavelength decreases, and because their period remains constant, their phase velocity C must also decrease. If sections of a single wave crest are traveling in different water depths, the sections in deeper water will travel further per unit time, and therefore the wave will change direction or refract. Wave height will first decrease slightly and then increase rapidly as still shallower water is reached. This increase is called shoaling. The combination of increasing wave height and decreasing wavelength leads to steeper waves which ultimately break. In addition, energy is dissipated due to bottom friction. The latter is not predicted by Airy theory, however, because it assumes an inviscid fluid. Finally, in selected situations, such as when waves pass a small island, diffraction occurs, which is a lateral transfer of energy along wave crests.

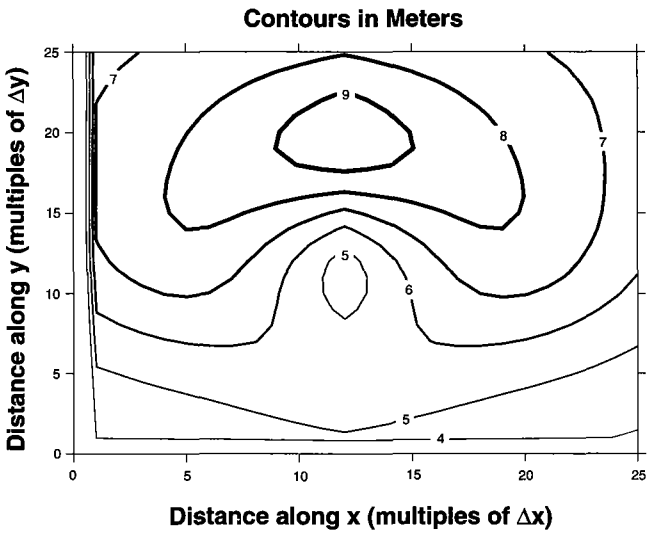

Figure 5-31
Experiment 5-8 computed significant wave heights at 1300 hours, September 4, 1973, under Tropical Storm Delia.

Here, we present a two-dimensional wave transformation program that accounts for refraction, shoaling, and breaking, but ignores diffraction and bottom friction. This is not severe because these last two processes are of lesser importance. The focus is not on wave crests but on wave *rays,* which are lines orthogonal to crests.

Deriving the model involves the path of the wave ray (Figure 5-32). By intuition, we know that the wave ray in Figure 5-32 must turn through some angle, $d\theta$, as the wave front crosses bottom contours obliquely. The front to the left of the ray travels through shallower water and therefore its phase velocity is slower than

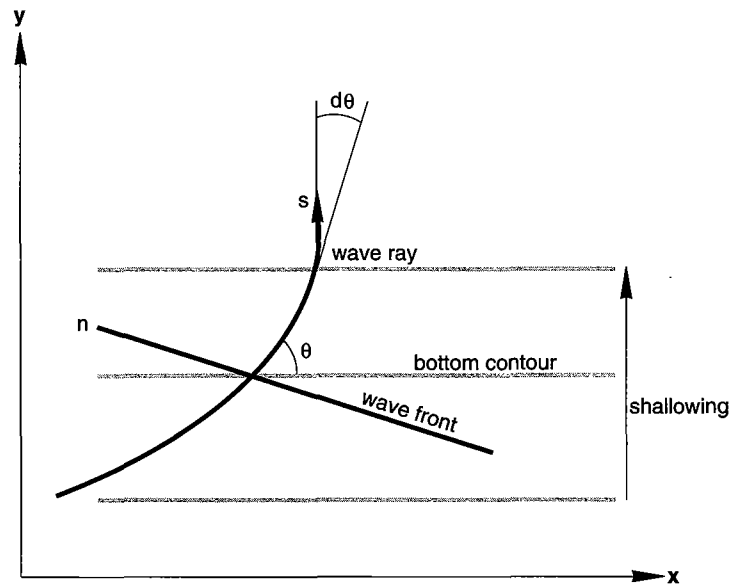

Figure 5-32
Definition sketch map for wave refraction in which ray of refracting wave propagates toward shore.

the front on the right. By geometry, the amount of turning per unit time is equal to the velocity gradient along the wave front, or:

$$\frac{d\theta}{dt} = \frac{dC}{dn} \tag{5-115}$$

By definition, $dt = ds/C$, and (5-115) can be written as:

$$\frac{d\theta}{ds} = \frac{1}{C}\frac{dC}{dn} \tag{5-116}$$

For the derivative with respect to n, it is easier to work in the x-y coordinate system. By trigonometry, (5-116) becomes:

$$\frac{d\theta}{ds} = \frac{1}{C}\left(\frac{\partial C}{\partial x}\sin\theta - \frac{\partial C}{\partial y}\cos\theta\right) \tag{5-117}$$

and:

$$\frac{dx}{dt} = C\cos\theta \quad \text{and} \quad \frac{dy}{dt} = C\sin\theta \tag{5-118}$$

Equations (5-117) and (5-118) provide the necessary relationships for calculating the path of an advancing wave ray through a field of variable phase velocity $C(x,y)$. You may ask how do we know the phase velocity as a function of x and y location? That comes from the celerity equation in Table 5-9, given water depth at each x- and y-coordinate pair.

As we might expect, there is no known analytical solution to (5-117) and (5-118) for an arbitrary phase velocity field, but numerous finite-difference solution schemes exist because the refraction problem is important in coastal oceanography and engineering. Here, we use a scheme of Koutitas (1988). The area of interest is discretized into rectangular cells Δx and Δy on a side (Figure 5-33). The finite difference form of (5-117) is:

$$\theta^{n+1} - \theta^n = \Delta s\left(\frac{1}{C^n}\left(\frac{\partial C^n}{\partial x}\sin\theta^n - \frac{\partial C^n}{\partial y}\cos\theta^n\right)\right) \tag{5-119}$$

where $\Delta s = \Delta t C^n$ and n refers to the nth node along the wave ray. The spatial derivatives of C are approximated as:

$$\frac{\partial C}{\partial x} = \frac{C_{i+1,j} - C_{i-1,j}}{\Delta x_i + \Delta x_{i-1}} \quad \text{and} \quad \frac{\partial C}{\partial y} = \frac{C_{i,j+1} - C_{i,j-1}}{\Delta y_j + \Delta y_{j-1}} \tag{5-120}$$

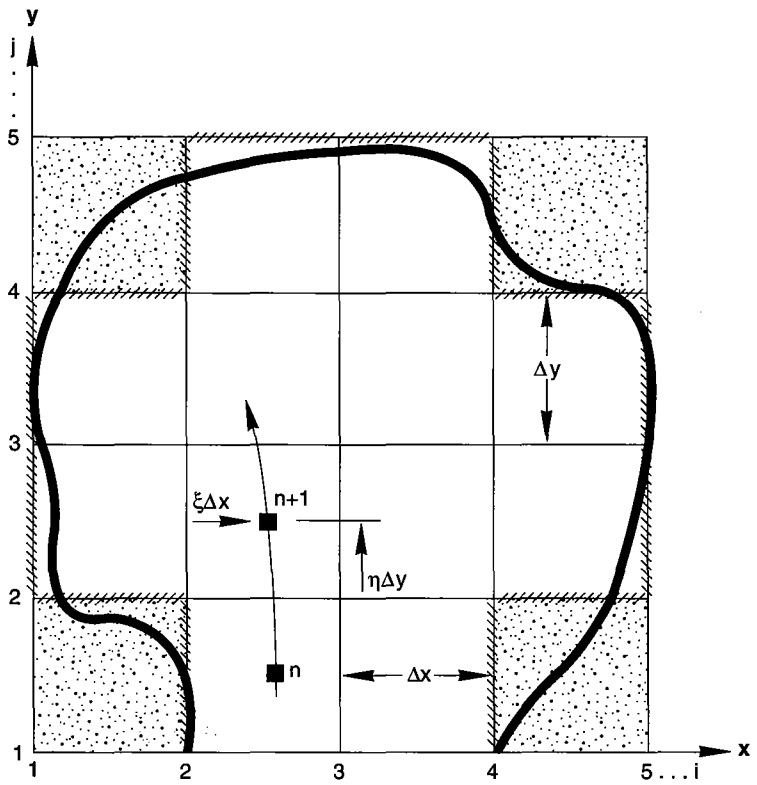

Figure 5-33 Finite-difference grid for wave refraction model.

Rarely will the location of the nth node coincide with the grid nodes, and therefore values of C and its gradients must be interpolated. Koutitas accomplishes this using the following function:

$$f^n = f_{i,j}(\zeta - 1)(\eta - 1) - f_{i+1,j}\zeta(\eta - 1) + f_{i+1,j+1}\zeta\eta + f_{i,j-1}\eta(\zeta - 1) \quad \textbf{(5-121)}$$

where ζ and η are defined in Figure 5-33.

Following computation of θ^{n+1}, the x and y location of the $n+1$ node is obtained from finite difference formulations of (5-118):

$$x^{n+1} = x^n + \Delta s \cos\left(\frac{\theta^n + \theta^{n+1}}{2}\right) \quad \textbf{(5-122)}$$

$$y^{n+1} = y^n + \Delta s \sin\left(\frac{\theta^n + \theta^{n+1}}{2}\right) \quad \textbf{(5-123)}$$

The preceding equations are encoded in FORTRAN in Program 23.

Experiment 5-9: Example of Wave Refraction

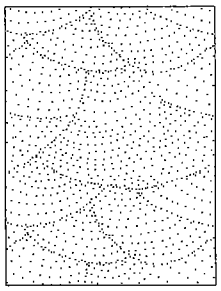

Even a casual observer of shorelines often notes that shores tend towards straight or smoothly curving arcs. This geometry stems in part from the effects of wave refraction, as the following example shows. Consider a hypothetical unconsolidated shoreline that consists of a sinusoidally corrugated surface plunging offshore at a few degrees, as shown in Figure 5-34. An offshore wave field approaches the coast with crests parallel to the average shoreline trend. They refract as they shoal, following rays computed in Program 23 using the input file in Table 5-12.

The results are plotted in Figure 5-34 as wave rays starting at selected sites offshore. Note that the headlands and corresponding offshore submarine highs refract the rays towards them, whereas the shoreline embayment repels the rays. Now remember Green's theorem (5-58), which states that if the total energy of a shallow water wave remains unchanged as it shoals, then its amplitude increases as the crest is compressed and water shallows. Applying Green's theorem to a wave segment defined by two rays, we see that wave energy is concentrated on the headlands and offshore shoals. The net effect is to erode sediment there and transport it to the embayments by longshore drift, thereby straightening the coastline through time.

Table 5-12 Experiment 5-9 data input file for wave refraction example.

```
im,jm,nm: # nodes in x and y; # computed orthogonals (I5) > 50<> 50<> 8<
Timestep in seconds (F10.3) and method of bathy entry > 10.0 < > 2<
dm (F10.3) > 50.0 <
deltax and deltay (F10.3) > 400.0 < > 400.0 <
Wave period and max # of apexes (F10.3 and I5) > 10.0 < > 500<
2000.0 1000.0 90.0
4000.0 1000.0 90.0
6000.0 1000.0 90.0
8000.0 1000.0 90.0
10000.0 1000.0 90.0
12000.0 1000.0 90.0
14000.0 1000.0 90.0
16000.0 1000.0 90.0
```

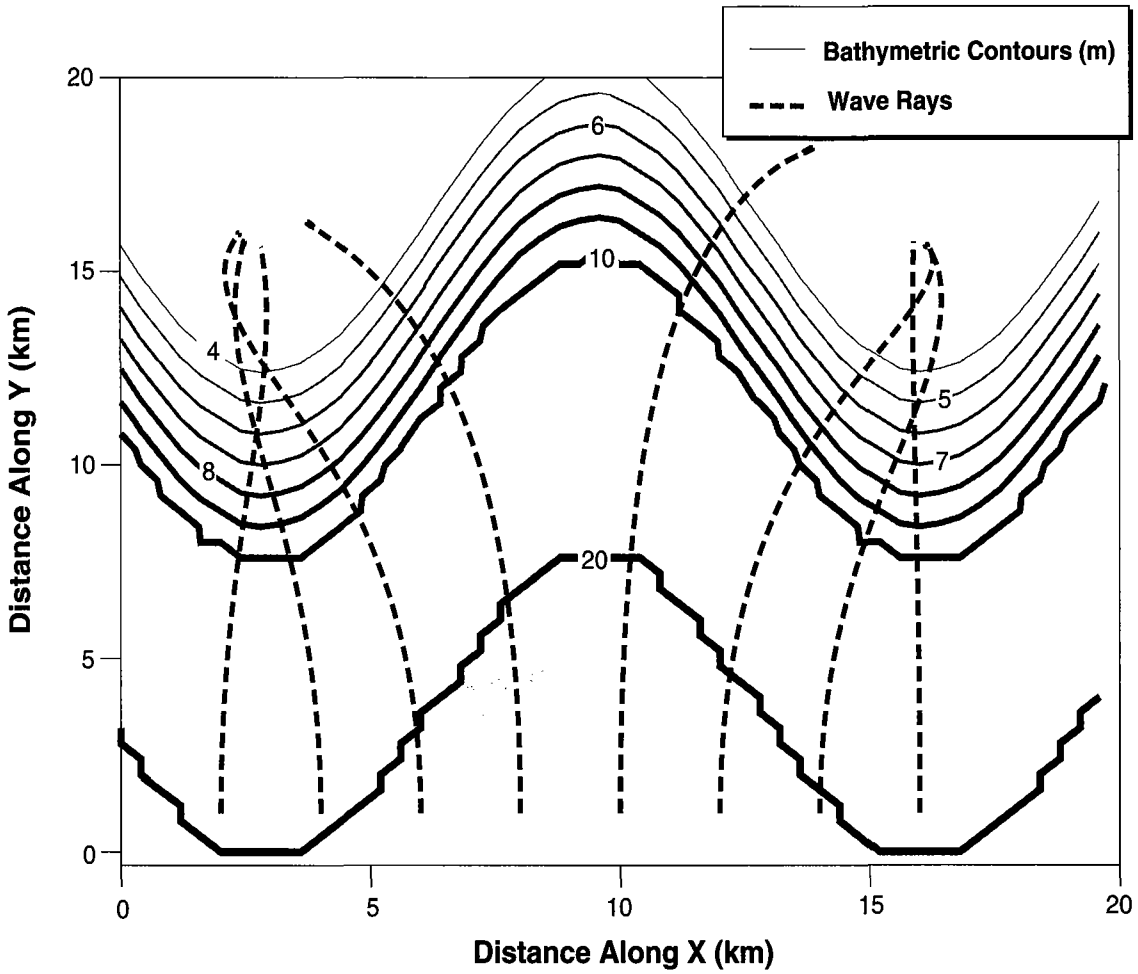

Figure 5-34 Wave rays refracting over sinusoidal sloping topography. Contour lines represent depths in meters.